CHAPTER 22

Overview of Multiscale Simulations of Materials

Gang Lu, Efthimios Kaxiras

Department of Physics and Division of Engineering and Applied Science, Harvard University, Cambridge, Massachusetts, USA

CONTENTS

1. INTRODUCTION

Some of the most fascinating problems in all fields of science involve multiple spatial or temporal scales: Processes that occur at a certain scale govern the behavior of the system across several (usually larger) scales. The notion and practice of multiscale modeling can be traced back to the beginning of modern science (see, e.g., the discussion in [1]). In many problems of materials science, this notion arises quite naturally: The ultimate microscopic constituents of materials are atoms, and the interactions among them at the microscopic level (on the order of nanometers and femtoseconds) determine the behavior of the material

at the macroscopic scale (on the order on centimeters and milliseconds and beyond), with the latter being the scale of interest for technological applications. The idea of performing simulations of materials across several characteristic length and timescales has, therefore, obvious appeal as a tool of potentially great effect on technological innovation [2–4]. The advent of ever-more-powerful computers that can handle such simulations provides further argument that such an approach can address realistic situations and can be a worthy partner to the traditional approaches of theory and experiment.

In the context of materials simulations, one can distinguish four characteristic length levels:

1. The atomic scale ($\sim 10^{-9}$/m or a few nanometers), in which the electrons are the players, and their quantum-mechanical state dictates the interactions among the atoms.
2. The microscopic scale ($\sim 10^{-6}$/m or a few micrometers), where atoms are the players and their interactions can be described by classical interatomic potentials (CIP) that encapsulate the effects of bonding between them, which is mediated by electrons.
3. The mesoscopic scale ($\sim 10^{-4}$/m or hundreds of micrometers), where lattice defects such as dislocations, grain boundaries, and other microstructural elements are the players. Their interactions are usually derived from phenomenological theories that encompass the effects of interactions between the atoms.
4. The macroscopic scale ($\sim 10^{-2}$/m or centimeters and beyond), where a constitutive law governs the behavior of the physical system, which is viewed as a continuous medium. In the macroscale, continuum fields such as density, velocity, temperature, displacement and stress fields, and so forth are the players. The constitutive laws are usually formulated so that they can capture the effects on materials properties from lattice defects and microstructural elements. Phenomena at each length scale typically have a corresponding timescale that, in correspondence to the four length scales mentioned above, ranges roughly from femtoseconds to picoseconds, to nanoseconds, to milliseconds and beyond.

At each length and timescale, well-established and efficient computational approaches have been developed over the years to handle the relevant phenomena. To treat electrons explicitly and accurately at the atomic scale, methods known as quantum Monte Carlo (QMC) [5] and quantum chemistry (QC) [6] can be employed, which are computationally too demanding to handle more than a few tens of electrons. Methods based on density-functional theory (DFT) and local density approximation (LDA) [7, 8] in its various implementations, although less accurate than QMC or QC methods, can be readily applied to systems containing several hundred atoms for static properties. Dynamical simulations with DFT methods are usually limited to timescales of a few picoseconds. For materials properties that can be modeled reasonably well with a small number of atoms (such as bulk crystal properties or point defects), the DFT approach can provide sufficiently accurate results. Recent progress in linear scaling electronic structure methods [9] has enabled DFT-based calculations to deal with a few thousand atoms (corresponding to sizes of a couple of nanometers on a side) with adequate accuracy. Finally, the semiclassical tight-binding approximation (TBA), although typically not as accurate as DFT methods, can extend the reach of simulations to a few nanometers in linear size and a few nanoseconds in timescale for the dynamics [10].

For material properties at the microscopic scale, molecular dynamics (MD) and Monte Carlo (MC) simulations are usually performed employing CIP, which can often be derived from DFT calculations [11, 12]. Although not as accurate as the DFT and TBA methods, the classical simulations are able to provide insight into atomic processes involving considerably larger systems, reaching up to $\sim 10^9$ atoms [13]. The timescale that MD simulations based on CIP can reach is up to a microsecond.

At the mesoscopic scale, the atomic degrees of freedom are not explicitly treated, and only larger-scale entities are modeled. For example, in what concerns the mechanical behavior of solids, dislocations are the objects of interest. In treating dislocations, recent progress has been concentrated on the so-called dislocation dynamics (DD) approach [14–17], which has come to be regarded as one of the most important developments in computational materials science and engineering in the last two decades [18]. Such DD models deal with the kinetics

of dislocations and can study systems a few tens of microns in size and with a maximum strain $\sim 0.5\%$ for a strain rate of 10 sec^{-1} in bcc metals [19].

Finally, for the macroscopic scale, finite-element (FE) methods [20] are routinely used to examine the large-scale properties of materials considered an elastic continuum [21]. For example, FE methods have been brought to bear on problems of strain-gradient plasticity, such as geometrically necessary dislocations [22]. Continuum Navier–Stoke equations are also often used to study fluids.

The challenge in modern simulations of materials science and engineering is that real materials usually exhibit phenomena on one scale that require a very accurate and computationally expensive description, and phenomena on another scale for which a coarser description is satisfactory and, in fact, necessary to avoid prohibitively large computations. Because none of the methods above alone would suffice to describe the entire system, the goal becomes to develop models that combine different methods specialized at different scales, effectively distributing the computational power where it is needed most. It is the hope that a multiscale approach is the answer to such a quest, and it is by definition an approach that takes advantage of the multiple scales present in a material and builds a unified description by linking the models at the different scales. Figure 1 illustrates the concept of a unified multiscale approach that can reach the length and timescale that individual methods, developed to treat a particular scale accurately, fail to achieve. At the same time, the unified approach can retain the accuracy that the individual approaches provide in their respective scales, allowing, for instance, for very high accuracy in particular regions of the systems as required. As effective theories, multiscale models are also useful for gaining physical insight that might not be apparent from brute force computations. Specifically, a multiscale model can be an effective way to facilitate the reduction and analysis of data, which sometimes can be overwhelming. Overall, the goal of multiscale approaches is to predict the performance and behavior of materials across all relevant length and timescales, striving to achieve a balance among accuracy, efficiency, and realistic description.

Conceptually, two categories of multiscale simulations can be envisioned, both sequential and concurrent. The sequential methodology attempts to piece together a hierarchy of computational approaches in which large-scale models use the coarse-grained representations with information obtained from more detailed, smaller-scale models. This sequential modeling approach has proven effective in systems in which the different scales are weakly coupled. The characteristic of the systems that are suited for a sequential approach is that the large-scale variations decouple from the small-scale physics, or the large-scale variations appear
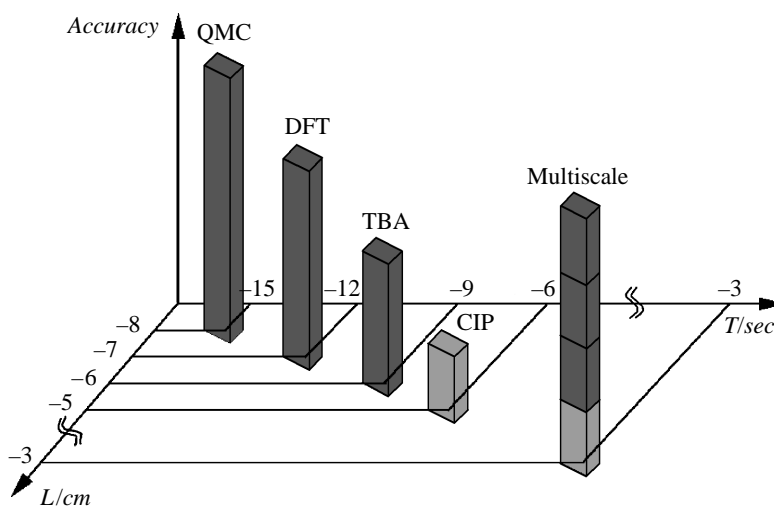
Figure 1. A schematic illustration of spacial and temporal scales achievable by various simulation approaches. The scales are in centimeters for the length dimension and seconds for the time dimension, both logarithmic. QMC, quantum Monte Carlo; DFT, density-functional theory; TBA, tight-binding approximation; CIP, classic interatomic potentials.

homogeneous and quasi-static from the small-scale point of view. Sequential approaches have also been referred to as serial, implicit, or message-passing methods. The vast majority of multiscale simulations that are actually in use is sequential. Examples of such approaches abound in literature, including almost all MD simulations whose underlying potentials are derived from electronic structure theory [23, 24], usually *ab initio* calculations [11, 12]. One frequently mentioned [25, 26] example of sequential multiscale simulations is the work of Clementi et al. [27], who used QC calculations to evaluate the interaction of several water molecules; from this database, an empirical potential was parameterized for use in MD simulations; the MD simulations were then used to evaluate the viscosity of water from atomic autocorrelation functions; and finally, the computed viscosity was employed in computational fluid dynamics calculations to predict the tidal circulation in Buzzard's Bay of Massachusetts.

The second category of multiscale simulations consists of the so-called concurrent, parallel, or explicit approaches. These approaches attempt to link methods appropriate at each scale together in a combined model, where the different scales of the system are considered concurrently and communicate with some type of hand-shaking procedure. This approach is necessary for systems that are inherently multiscale; that is, systems whose behavior at each scale depends strongly on what happens at the other scales. In contrast to sequential approaches, the concurrent simulations are still relatively new, and only a few models have been developed to date. In a concurrent simulation, the system is often partitioned into domains characterized by different scales and physics. The challenge of the concurrent approach lies at the coupling between the different regions treated by different methods; a successful multiscale model seeks a smooth coupling between these regions.

In principle, multiscale simulations could be based on a hybrid scheme, using elements from both the sequential and the concurrent approaches. We will not examine this type of approach in any detail, as it involves no new concepts other than the successful combination of elements underlying the other two types of approaches.

There already exist a few review papers and special editions of articles on multiscale simulation of materials in the literature [2, 3, 28–32]. A mathematic perspective of multiscale modeling and computation is also available [33]. The present overview does not aim to provide another collection of various multiscale techniques but, rather, to identify the characteristic features and classify multiscale simulation approaches into rational categories in relation to the problems where they apply. We select a few illustrative examples for each category and try to establish connections between these approaches whenever possible. Because almost all interesting material behavior and processes are time dependent, we will address both the issue of length scales and the issue of timescales integration in materials modeling.

The examples presented in this overview to some extent reflect our own research interests, and they are by no means exhaustive. Nevertheless, we hope that they give a satisfactory cross section of the current state of the field and that they can serve as inspiration for further developments in this exciting endeavor.

2. SEQUENTIAL MULTISCALE APPROACHES

Two ingredients are required to construct a successful sequential multiscale model: first, it is necessary to have *a priori* and complete knowledge of the fundamental processes at the lowest scale involved. This knowledge or information can then be used for modeling the system at successively coarser scales. Second it is necessary to have a reliable strategy for encompassing the lower-scale information into the coarser scales. This is often accomplished by phenomenological theories, which contain a few key parameters (these can be functions), the value of which is determined from the information at the lower scale. This message-passing approach can be performed in sequence for multiple-length scales, as in the example cited in the introduction [27]. The key attribute of the sequential approach is that the simulation at a higher level critically depends on the completeness and the correctness of the information gathered at the lower level, as well as the efficiency and reliability of the model at the coarser level.

To illustrate this type of approach, we will present two examples of sequential multiscale approaches in some detail. The first example concerns the modeling of dislocation properties

in the context of the Peierls–Nabarro (P-N) phenomenological model, where the lower scale information is in the form of the so-called generalized stacking fault energy surface (also referred to as the γ-surface) and the coarse-grained model is a phenomenological continuum description. The second example concerns the modeling of coherent phase transformations in the context of the phase-field approach, where the lower scale knowledge is in the form of *ab initio* free energies and the coarse-grained model is again a continuum model.

2.1. Peierls–Nabarro Model of Dislocations

Dislocations are central to our understanding of mechanical properties of crystalline solids. In particular, the creation and motion of dislocations mediate the plastic response of a crystal to external stress. Although continuum elasticity theory describes well the long-range elastic strain of a dislocation for length scales beyond a few lattice spacings, it breaks down in the immediate vicinity of the dislocation core. There has been a great deal of interest in accurately describing the dislocation core structure on an atomic scale because the core structure to a large extent dictates the dislocation properties [34, 35]. So far, direct atomistic simulation of dislocation properties based on CIP has not been satisfactory because the CIP is not always reliable, or may even not be available for the material of interest, especially when the physical system involves several types of atoms. However, *ab initio* calculations are still computationally expensive for the study of dislocation core properties, particularly for that of dislocation mobility. Recently, a promising approach based on the framework of the P-N model has attracted considerable interest in the study of dislocation core structure and mobility [36–47]. This approach, when combined with *ab initio* calculations for the energetics, represents a plausible alternative to the direct *ab initio* simulations of dislocation properties.

The P-N model is an inherently multiscale framework, first proposed by Peierls [48] and Nabarro [49] to incorporate the details of a discrete dislocation core into a framework that is essentially a continuum. Consider a solid with an edge dislocation in the middle (Fig. 2): the solid containing this dislocation is represented by two elastic half-spaces joined by atomic-level forces across their common interface, known as the glide plane (dashed line). The goal of the P-N model is to determine the slip distribution on the glide plane, which minimizes the total energy. The dislocation is characterized by the slip (relative displacement) distribution

$$\mathbf{f}(x) = \mathbf{u}(x, 0^+) - \mathbf{u}(x, 0^-) \tag{1}$$

which is a measure of the misfit across the glide plane; $\mathbf{u}(x, 0^+)$ and $\mathbf{u}(x, 0^-)$ are the displacement of the half-spaces at position x immediately above and below the glide plane.
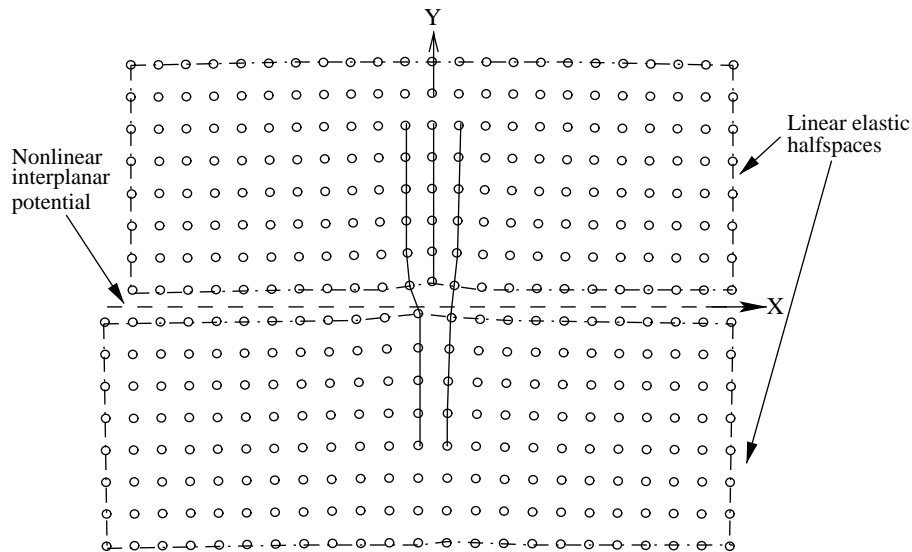
Figure 2. A schematic illustration showing an edge dislocation in a lattice. The partition of the dislocated lattice into a linear elastic region and a nonlinear atomistic region allows a multiscale treatment of the problem.

The total energy of the dislocated solid includes two contributions: the nonlinear potential energy resulting from the atomistic interaction across the glide plane, and the elastic energy stored in the two half-spaces associated with the presence of the dislocation. Both energies are functionals of the slip distribution $\mathbf{f}(x)$. Specifically, the nonlinear misfit energy can be written as

$$U_{\text{misfit}} = \int_{-\infty}^{\infty} \gamma[\mathbf{f}(x)]\, dx \tag{2}$$

where $\gamma(\mathbf{f})$ is the generalized stacking fault energy surface (the γ-surface) introduced by Vitek [50]. The nonlinear interplanar γ-surface can, in general, be determined from atomistic calculations. For systems in which CIP are not available or not reliable (e.g., it is exceedingly difficult to derive reliable potentials for multicomponent alloys), *ab initio* calculations can be performed to obtain the γ-surface. However, the elastic energy of the dislocation can be calculated reasonably from elasticity theory: The dislocation may be thought of as a continuous distribution of infinitesimal dislocations whose Burgers vectors integrate to that of the original dislocation [51]. Therefore, the elastic energy of the original dislocation is just the sum of the elastic energy caused by all the infinitesimal dislocations (from the superposition principle of linear elasticity theory), which can be written as

$$U_{\text{elastic}} = \frac{\mu}{2\pi(1-\nu)} \int dx \int dx' \ln \frac{L}{|x-x'|} \frac{d\mathbf{f}(x)}{dx} \frac{d\mathbf{f}(x')}{dx'} \tag{3}$$

where μ and ν are the shear modulus and Poisson's ratio, respectively. The variable L is an inconsequential constant introduced as a large-distance cutoff for the computation of the logarithmic interaction energy [52]. Note that the Burgers vector of each infinitesimal dislocation is the local gradient in the slip distribution $d\mathbf{f}(x)/dx$. The gradient of $\mathbf{f}(x)$ is called dislocation (misfit) density, denoted by $\rho(x)$. Because the P-N model requires that atomistic information (embodied in the γ-surface) be incorporated into a coarse-grained continuum framework, it is a sequential multiscale strategy. Thus, the successful application of the method depends on the reliability of both γ-surface and the underlying elasticity theory, which is the basis for the formulation of the phenomenological theory.

In the current formulation, the total energy is a function of misfit distribution $\mathbf{f}(x)$ or, equivalently, $\rho(x)$, and it is invariant with respect to arbitrary translation of $\rho(x)$ and $\mathbf{f}(x)$. To regain the lattice discreteness, the integration of the γ-energy in Eq. (2) was discretized and replaced by a lattice sum in the original P-N formulation

$$U_{\text{misfit}} = \sum_{i=-\infty}^{\infty} \gamma(\mathbf{f}_i)\Delta x \tag{4}$$

with x_i the reference position and Δx the average spacing of the atomic rows in the lattice. This procedure, however, is inconsistent with evaluation of elastic energy [Eq. (3)] as a continuous integral. Therefore, the total energy is not variational. Furthermore, in the original P-N model, the shape of the solution $\mathbf{f}(x)$ is assumed to be invariant during dislocation translation, a problem that is also associated with the nonvariational formulation of the total energy.

To resolve these problems, a so-called semidiscrete variational P-N (SVPN) model was recently developed [43] that allows for the first time the study of narrow dislocations, a situation that the standard P-N model can not handle. Within this approach, the equilibrium structure of a dislocation is obtained by minimizing the dislocation energy functional

$$U_{\text{disl}} = U_{\text{elastic}} + U_{\text{misfit}} + U_{\text{stress}} + Kb^2 lnL \tag{5}$$

where

$$U_{\text{elastic}} = \sum_{i,j} \frac{1}{2} \chi_{ij} \left[K_e \left(\rho_i^{(1)} \rho_j^{(1)} + \rho_i^{(2)} \rho_j^{(2)} \right) + K_s \rho_i^{(3)} \rho_j^{(3)} \right] \tag{6}$$

$$U_{\text{misfit}} = \sum_i \Delta x \gamma_3(\mathbf{f}_i) \tag{7}$$

$$U_{\text{stress}} = -\sum_{i,l} \frac{x_i^2 - x_{i-1}^2}{2} (\rho_i^{(l)} \tau_i^{(l)}) \tag{8}$$

with respect to the dislocation misfit density. Here, $\rho_i^{(1)}$, $\rho_i^{(2)}$, and $\rho_i^{(3)}$ are the edge, vertical, and screw components of the general interplanar misfit density at the ith nodal point, respectively, and $\gamma_3(\mathbf{f}_i)$ is the corresponding three-dimensional γ-surface. The components of the applied stress interacting with the $\rho_i^{(1)}$, $\rho_i^{(2)}$, and $\rho_i^{(3)}$ are $\tau^{(1)} = \sigma_{21}$, $\tau^{(2)} = \sigma_{22}$, and $\tau^{(3)} = \sigma_{23}$, respectively. The variables K, K_e, and K_s are the prelogarithmic elastic energy factors [52]. The dislocation density at the ith nodal point is $\rho_i = (f_i - f_{i-1})/(x_i - x_{i-1})$, and χ_{ij} is the elastic energy kernel [43].

The first term in the energy functional U_{elastic} is now discretized to be consistent with the discretized misfit energy, which makes the total energy functional variational. Another modification in this approach is that the nonlinear misfit potential in the energy functional U_{misfit} is a function of all three components of the nodal misfit $\mathbf{f}(x_i)$. Namely, in addition to the misfit along the Burgers vector, lateral and even vertical misfits across the glide plane are also included. This allows the treatment of straight dislocations of arbitrary orientation in arbitrary glide planes. Furthermore, because the misfit vector $\mathbf{f}(x_i)$ is allowed to change during the process of dislocation translation, the energy barrier (referred to as the Peierls barrier) can be significantly lowered compared to the corresponding value taken from a rigid translation. The response of a dislocation to an applied stress is achieved by minimization of the energy functional with respect to ρ_i at the given value of the applied stress, $\tau_i^{(l)}$. An instability is reached when an optimal solution for ρ_i no longer exists, which is manifested numerically by the failure of the minimization procedure to converge. The Peierls stress is defined as the critical value of the applied stress that gives rise to this instability.

The SVPN model has been applied to study various interesting material problems related to dislocation phenomena [45–47]. One study involved the understanding of hydrogen-enhanced local plasticity (HELP) in Al. HELP is regarded as one of three general mechanisms responsible for H embrittlement of metals [53]. There was overwhelming experimental evidence in support of HELP, but a theoretical foundation was lacking. To gain an understanding of the physics behind the HELP mechanism, Lu et al. carried out *ab initio* calculations for the γ-surface of Al with H impurities placed at the interstitial sites [45]. The γ-surfaces for both pure Al and the Al + H systems are shown in Fig. 3. Comparing the two γ-surfaces, one finds an overall reduction in γ-energy in the presence of H, which is attributed to the change of atomic bonding across the glide plane, from covalent-like to ionic-like [54].
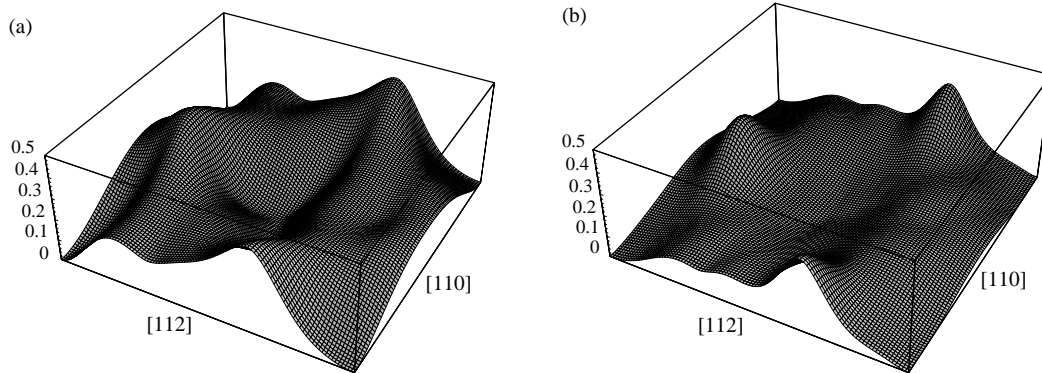
Figure 3. The γ-surface (J/m^2) for displacements along a (111) plane for (a) pure Al and (b) Al + H systems. The corners of the plane and its center correspond to identical equilibrium configurations (i.e., the ideal lattice). The two surfaces are displayed in exactly the same perspective and on the same energy scale to facilitate comparison of important features.

The core properties of four different dislocations, screw (0°), 30°, 60°, and edge (90°) have been studied using the SVPN model combined with the *ab initio*–determined γ-surface. It was found that the Peierls stress for these dislocations is reduced by more than an order of magnitude in the presence of H [45], which is compatible with the experimental findings that support the HELP mechanism [53]. Moreover, to address the experimental observation for H trapping at dislocation cores and H-induced slip planarity, the H-binding energy to the dislocation cores was calculated [45]. These calculations showed that there is strong binding between H and the dislocation cores; that is, H is attracted (trapped) to dislocation cores, which lowers the core energies. More important, the binding energy was found to be a function of dislocation character, with the edge dislocation having the greatest and the screw dislocation having the lowest binding energies. For a mixed dislocation, the binding energy increases with the amount of edge component of the Burgers vector. These results indicate that in the presence of H, it costs more energy for an edge dislocation to transform into a screw dislocation to cross-slip, as the edge dislocation has almost twice the binding energy of the screw dislocation [45]. In the same vein, it costs more energy for a mixed dislocation to transfer its edge component to a screw component for cross-slip. Therefore, the cross-slip process is suppressed because of the presence of H, and the slip is confined to the primary glide plane, exhibiting the experimentally observed slip planarity.

A similar approach was applied to the study of the vacancy lubrication effect on dislocation motion in Al. From this analysis, it was shown that the role of vacancies is crucial in reconciling the results of Peierls stress measured from different experimental techniques [46]. Very recently, a multiple-plane P-N model has been developed to study dislocation phenomena involving more than one glide plane, such as dislocation constriction and cross-slip [47]. Finally, we should point out that the P-N model is just one example of more-general cohesive surface models that are built on the idea of limiting all constitutive nonlinearity to certain privileged interfaces, while the remainder of the material is treated via more conventional continuum theories [1]. The same strategy can also be applied to the study of fracture and dislocation nucleation from a crack tip [55].

It is interesting to note that the analysis of γ-surface can provide a qualitative understanding of even more complex mechanical properties of materials. For example, Rice and coworkers [56] formulated powerful criteria for the brittle behavior of materials by extending the Peierls analysis to geometries involving cracks. Based on this framework, Waghmare et al. [57, 58] were able to predict which alloying elements could improve the ductility of $MoSi_2$ by analyzing the *ab initio*–determined γ-surface of the alloys and comparing the changes induced by alloying to key features of the γ-surface to the induced changes of the surface energy γ_s. Remarkably, certain predictions of this relatively simple theoretical modeling were borne out by subsequent experiments [59].

We have devoted some attention to the description of the P-N model and its implementation using *ab initio* γ-surfaces because it is an ideal case of a sequential multiscale model: It consists of a well-motivated phenomenological framework, within which the set of atomistically derived quantities is well defined and complete (in this case, the γ-surface). In this sense, it fulfills all the requirements for a coherent and complete multiscale model. There are, no doubt, limitations to the model, arising from the range of validity of the phenomenological theory, but within this range there are no other ambiguities in constructing the multiscale model. Perhaps its successes, some of which we presented above, are owed to this complete character of the model.

2.2. Phase-Field Model of Coherent Phase Transformations

The structure–properties paradigm is one of the principal pillars in materials science. The term *structure* here refers to structures at many different scales, including the atomic-scale geometry determined by the crystalline arrangement of atoms, the structure of the defects that exist in a material, and the structure that emerges as a result of the organization of these defects into what is referred to as microstructure. Among these structures, the microstructure on the scale of micrometers is often directly tied to the mechanical properties of materials, and it has therefore attracted great interest in terms of both scientific understanding and practical applications [60–64].

Recently, a powerful sequential multiscale approach has been put forward for modeling the precipitate microstructure and its evolution in multicomponent alloys [65, 66], materials that appear in many technological applications. The approach is based on the continuum phase-field model whose driving forces (free energies) are obtained from combined *ab initio* calculations and the mixed-space cluster expansion technique. One interesting application of this approach concerned the study of precipitation of the $\theta'(Al_2Cu)$ phase in Cu–Al alloys during thermal aging [66].

In the phase-field multiscale approach, the nature of phase transformation as well as the microstructures that are produced are described by a set of continuous order–parameter fields [67, 68]. The temporal microstructure evolution is obtained from solving field kinetic equations that govern the time-dependence of the spatially inhomogeneous order–parameter fields. Within the diffuse-interface description, the thermodynamics of a phase transformation and the accompanying microstructure evolution are modeled by a free energy that is a function of the order–parameter field, or phase field. For a structural transformation, the total free energy can be written as

$$\mathscr{F}_{\text{tot}} = \mathscr{F}_{\text{bulk}} + \mathscr{F}_{\text{inter}} + \mathscr{F}_{\text{elast}} \tag{9}$$

where $\mathscr{F}_{\text{bulk}}$ is the bulk free energy, $\mathscr{F}_{\text{inter}}$ is the interfacial free energy, and $\mathscr{F}_{\text{elast}}$ is the coherency elastic-strain energy arising from the lattice accommodation along the coherent interfaces in a microstructure. For a microstructure described by a composition field c and a set of structural order–parameters $\eta_1, \ldots, \eta_p$, the first two terms of Eq. (9) are given by

$$\mathscr{F}_{\text{bulk}} + \mathscr{F}_{\text{inter}} = \int_V \left\{ f[c(\mathbf{r}), \eta_p(\mathbf{r})] + \frac{\alpha}{2} |\nabla c(\mathbf{r})|^2 + \frac{1}{2} \sum_p \beta_{ij}(p) \nabla_i \eta_p(\mathbf{r}) \nabla_j \eta_p(\mathbf{r}) \right\} dV \tag{10}$$

where $f(c, \eta_p)$ is the local free-energy density [69] and α and $\beta_{ij}(p)$ are the gradient energy coefficients that control the width of the diffuse interface. The elastic-strain energy is obtained from elasticity theory using the homogeneous modulus approximation [70]. With the total free energy of an inhomogeneous system written as a function of order–parameter fields, the temporal evolution of microstructures during a phase transformation can be obtained by solving the coupled Cahn–Hilliard equation for a conserved field c, and the time-dependent Ginzburg–Landau equation for a nonconserved field η_p [71, 72].

$$\frac{\partial c}{\partial t} = M \nabla^2 \left(\frac{\partial f}{\partial c} - \alpha \nabla^2 c \right) \tag{11}$$

$$\frac{\partial \eta_p}{\partial t} = -L_p \frac{\delta \mathscr{F}_{\text{tot}}}{\delta \eta_p} \tag{12}$$

where M is related to atom mobility and L_p is the relaxation constant associated with the order–parameter η_p. As the above equations illustrate, the continuum phase-field methodology depends on three input energies: bulk free energies of solid solution and precipitate phases, precipitate–matrix interfacial free energies, and precipitate–matrix lattice elastic energies. Experimental determination of these quantities can be difficult and problematic. Therefore, a physically motivated method for accurately determining these quantities is of critical importance for predicting the microstructure evolution of interest. In particular, if the quantities can be determined from *ab initio* calculations, the goal of an *ab initio* modeling of alloy microstructure evolution would be, to a great extent, achieved [73, 74].

Because direct *ab initio* calculations of free energies are either impractical or impossible with the currently available computational power, a useful method has been developed to extend the *ab initio* energetics to thermodynamic properties of alloy systems with hundreds of thousands of atoms [75], referred to as the mixed-space cluster expansion (CE). In this scheme, energetics from *ab initio* calculations for a number of small–unit cell ($\sim$10 atoms) structures are mapped onto a generalized Ising-like model for a particular lattice type, involving two-, three-, and four-body interactions plus coherency strain energies [76]. The Hamiltonian can be incorporated into mixed-space Monte Carlo simulations of $N \sim 10^5$ atoms, effectively allowing one to explore the complexity of 2^N configurational

space. As demonstrated by Vaithyanathan et al. [66] the bulk free energy can be obtained from Monte Carlo simulations coupled with thermodynamic integration techniques. The precipitate–matrix interfacial free energies can be determined from similar Monte Carlo simulations or from low-temperature expansion techniques. The elastic strain energies are of precisely the same form as the coherency strain energy used to generate the mixed-space CE. Hence, from a combination of *ab initio* calculations, a mixed-space CE approach, and Monte Carlo simulations, one can obtain all the driving forces needed as input to the continuum phase-field model. The incorporation of these energetic properties, obtained from atomistics, into a continuum microstructural model represents a bridge between these two length scales and opens the path toward predictive modeling of microstructures and their evolution.

To illustrate the use of the method, we mention briefly the work of Vaithyanathan et al. [66], who studied the problem of precipitation of the θ' (Al_2Cu) phase in Cu–Al alloys. The free energy of the θ' phase is obtained from *ab initio* calculations of the energy at $T = 0$ K, coupled with the calculated vibrational entropy of this phase. The bulk free energies of matrix and precipitate phases are then fit to the local free energy as a function of order–parameter fields in the phase-field model. From supercell calculations, $T = 0$ K interfacial energies are determined, both for the coherent interface and for the incoherent interface. The anisotropy of these interfacial energies is large and has been incorporated in the phase-field model. Elastic energy calculations for the coherent strain of Al/Al_2Cu (θ') and the calculated lattice parameters of each phase determine the elastic driving force in this system. Having determined all the necessary thermodynamic input, Vaithyanathan et al. [66] were able, for the first time, to clarify the physical contributions responsible for the observed morphology of θ' precipitate microstructure. The agreement between the calculated and the experimentally observed microstructures of θ' in the Al–Cu alloys was excellent, confirming the validity of the approach.

Although the phase-field model is able to predict complex microstructure evolution during phase transformations, it requires, as input, phenomenological thermodynamic and kinetic parameters. For binary systems, *ab initio* calculations can provide these parameters for the phase-field model, but it is unrealistic to assume that such calculations can be used to determine all the thermodynamic information for systems beyond ternary. Therefore, semiempirical methods, such as CALPHAD (calculated phase-diagram) will remain a useful tool in such an endeavor [77–79].

2.3. Other Sequential Approaches

Kinetic Monte Carlo (KMC) simulations, coupled with atomistically determined kinetic energy barriers, represent a powerful class of sequential multiscale approaches. For example, a large body of research has been carried out into surface-growth phenomena with KMC simulations whose kinetic energy barrier parameters for relevant elemental processes are supplied by *ab initio* calculations [80, 81]. In an altogether different field, Cai et al. [82] have used the KMC method to study dislocation motion in Si based on the well-established double-kink mechanism. In their approach, the dislocation is represented by a connected set of straight-line segments that move as the cumulative effect of a large number of kink nucleation and migration processes. The rate of these processes is calculated from transition state theory, with the transition energy barrier having contributions from both atomistically determined energetics (double-kink formation and migration energy) and elastic interactions with other dislocation segments, as well as from the externally applied stress.

An example of a multiscale approach, in which KMC is a key component, employs the so-called level-set method [83, 84] for the largest (macroscopic) scale. This approach is particularly well suited for the study of epitaxial growth, a subject of great importance in microelectronics and optoelectronics applications. In the level-set method, growth is described by the creation and subsequent motion of island boundaries. The model treats the growing film as a continuum in the lateral direction but retains atomistic discreteness in the growth direction. In the lateral direction, continuum equations representing the field variables can be coupled to growth through island evolution by solving the appropriate boundary-value problem for the field and using local values of this field to determine the velocity of the island boundaries. The central idea behind the level-set method [85] is that any boundary

curve Γ, such as a step or the boundary of an island, can be represented as the set of values $\varphi = 0$ (the level-set) of a smooth function φ. For a given boundary velocity v, the equation for φ is

$$\frac{\partial \varphi}{\partial t} + \mathbf{v} \cdot \nabla \varphi = 0 \qquad (13)$$

Growth is naturally described by the smooth evolution of φ, determined by this differential equation. In the case of multilayer growth, the boundaries $\Gamma_k(t)$ of the islands are defined as the set of spatial points x for which $\varphi(\mathbf{x}, t) = k$ for $k = 0, 1, 2$, and so on. The evolution of the level-set function φ can be obtained by numerically solving Eq. (13) using nonoscillatory methods [86]. The key parameters entering the model are diffusion constants (the terrace and island-edge diffusion constants) that can, in principle, be supplied from atomistic calculations through the following procedure (see Fig. 4): first, the atomistic processes that are responsible for terrace or island-edge diffusion are identified and their energetics analyzed using atomistic (possibly *ab initio*) calculations; next, the energy barriers for the atomistic processes are incorporated in a KMC model that provides the means for coarse-graining the atomistic degrees of freedom to a few mesoscopic degrees of freedom, describing the evolution of surface features (the island step edges); finally, the results of the KMC model are coarse-grained to provide the input to the level-set equations—that is, they define the values of the boundary velocity $\mathbf{v}$, which depends on the local surface morphology. The coarse-graining between scales eliminates degrees of freedom that are not essential, making the passage to the next scale feasible. For example, in the illustration shown in Fig. 4, the smallest step width in the KMC scale corresponds to a two-atom-wide region at the microscopic scale, a situation that is relevant to the Si(100) surface and possibly to other semiconductor surfaces (such as III–V compound surfaces). In these cases, surface atoms tend to be bound to dimer pairs, which is the essential unit that determines the step structure, even though the underlying dynamics may be determined by the motion of individual atoms. Thus, the KMC simulation need only take into account structures consisting of dimer units, the dynamics of which determine the step-edge motion needed for the level-set simulation. The middle terrace in Fig. 4(b) is shown as a grid of squares, each representing a four-atom cluster and being the minimal unit relevant to step motion at the KMC scale in this example, assuming that only steps of width equal to two atoms in each direction are stable. The level-set method is a manifestly multiscale approach, combining information from three different
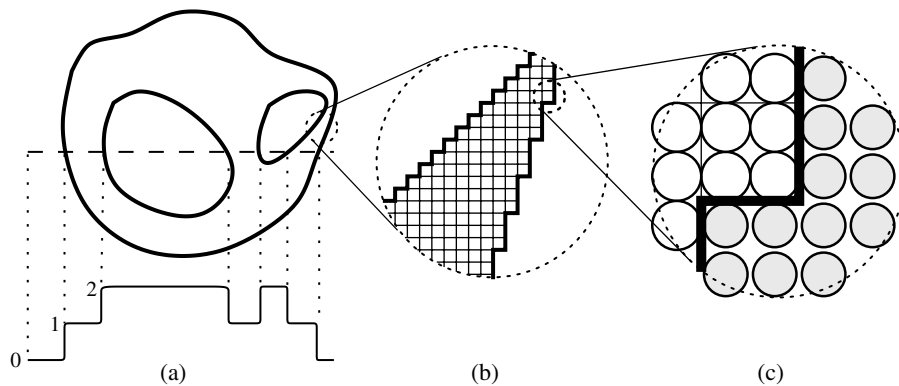
Figure 4. Illustration of the three different levels of simulation in the level-set multiscale approach of surface growth. (a) The macroscopic scale, in which island borders are continuous lines separating heights at different levels (the levels along a particular cross section are shown schematically, labeled 0, 1, and 2); this scale is treated with the level-set method. (b) The mesoscopic scale, where the features of the island edges contain some information about the underlying atomic lattice, indicated here as the small straight lines that define step directions consistent with atomic positions; this scale is treated with the kinetic Monte Carlo approach. (c) The microscopic scale, where the individual degrees of freedom are explicitly included. The step is determined by the positions of atoms in two terraces, with the ones on the upper terrace shown as white larger circles and the ones on the lower terrace shown as shaded smaller circles; this scale is treated by atomistic (possibly *ab initio*) methods. All views in this schematic representation are top views (see text for details).

regimes (atomistic, mesoscopic, and continuum) into a neatly integrated scheme. Recently, the level-set method has also been applied to study dislocation dynamics in alloys [87].

Yet another sequential multiscale approach has been successfully applied to the study of crystal plasticity. This is the DD method mentioned earlier, which incorporates dislocation motion at the macroscopic scale—the mechanism ultimately responsible for crystal plasticity. To predict the mechanical properties of materials using DD simulations, a connection between micro-to-meso scales must be established because dislocation interactions at close range (when the cores intersect, for instance) are totally beyond the reach of continuum models. Along these lines, Bulatov et al. were able to study dislocation reactions and plasticity in fcc metals [88] that compare well with deformation experiments by integrating the local rules derived from atomistic simulation of dislocation core interactions into the DD simulations. The same idea has been further explored by Rhee et al. in a study of the stage I stress–strain behavior of bcc single crystals [19].

3. CONCURRENT MULTISCALE APPROACHES

Broadly speaking, a concurrent multiscale approach is more general in scope than its sequential counterpart because the concurrent approach does not rely on any assumptions (in the form of a particular coarse-graining model) pertaining to a particular physical problem. As a consequence, a successful concurrent approach can be used to study many different problems. For example, dislocation core properties, grain boundary structure, and crack propagation could all be modeled individually or collectively by the same concurrent approach, as long as it incorporates all the relevant features at each level. What is probably most appealing, however, is that a concurrent approach does not require *a priori* knowledge of the physical quantities or processes of interest. Thus, concurrent approaches are particularly useful when exploring problems about which little is known at the atomistic level and about their connection to larger scales, and when discovering new phenomena. We discuss below three instances of concurrent approaches in some detail and mention some additional examples more briefly.

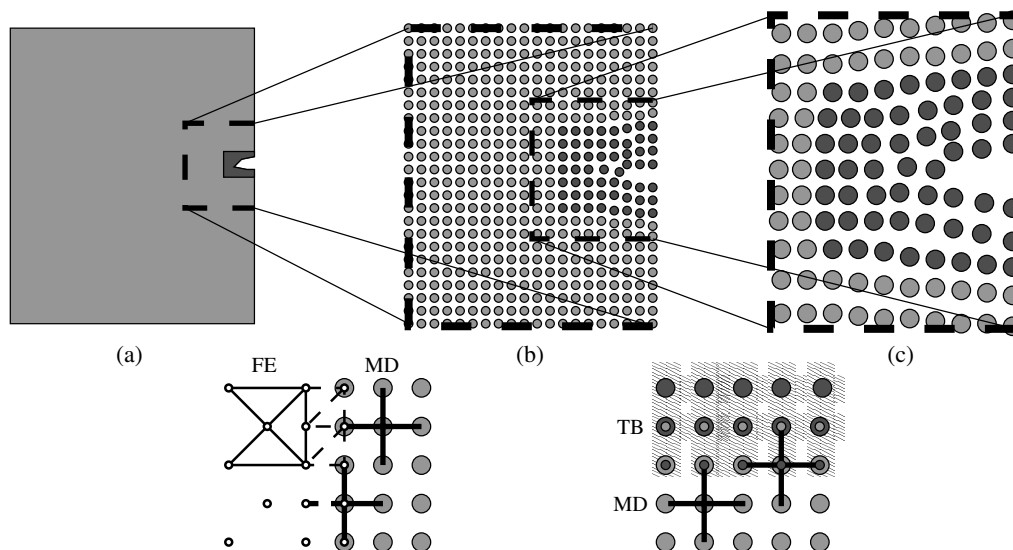### 3.1. Macroscopic Atomistic *Ab Initio* Dynamics

Fracture dynamics is one of the most challenging problems in materials science and solid mechanics. Despite nearly a century of study, several important issues remain unsolved. In particular, there is little fundamental understanding of the brittle-to-ductile transition as a function of temperature in materials, there is still no definitive explanation of how fracture stress is transmitted through plastic zones at crack tips, and there is no complete understanding of the disagreement between theory and experiment regarding the limiting speed of crack propagation. These difficulties stem from the fact that fracture phenomena are governed by processes occurring over a wide range of length scales that are all connected and that all contribute to the total fracture energy [89]. In particular, the physics on different length scales interacts dynamically; therefore, a sequential coupling scheme would not be adequate for the study of fracture dynamics.

To address these challenges, Abraham, Broughton, Bernstein, and Kaxiras developed a concurrent multiscale modeling approach that dynamically couples different length scales [25, 26]. This multiscale methodology aims at linking the length scales ranging from the atomic scale, treated with a quantum-mechanical tight-binding approximation method; through the microscale, treated via the classical molecular dynamics method; and finally to the mesoscale/macroscale, treated via the finite element method in the context of continuum elasticity. These authors applied this unified approach, termed macroscopic-atomistic–*ab initio* dynamics (MAAD), to the study of the dynamical fracture process in Si, a typical brittle material. In traditional studies of fracture, only the continuum mechanics level (employing, for instance, the FE method) is usually invoked to account for the macroscopic behavior. However, as there is no natural small-length cutoff present in the continuum mechanics approach, any important aspect of the atomic-scale mechanisms for fracture is completely missed. This can be remedied by introducing classical MD to the simulations.

In particular, the MAAD approach employed the Stillinger–Weber [90] interatomic empirical potential for Si to perform MD calculations at the atomistic level for a large region of the material near a crack tip. However, the treatment of formation and the breaking of covalent bonds at the atomic scale is not reliable with any empirical potential, because bonds between atoms are an essentially quantum mechanical phenomenon arising from the sharing of valence electrons. However, small deviations from ideal bonding arrangements can be captured accurately by empirical potentials because they are, to first approximation, harmonic, a feature that is easily incorporated in empirical descriptions of the interaction between atoms. Therefore, it was deemed necessary to include a quantum mechanical approach in the simulations of a small region in the immediate neighborhood of the crack tip, where bond breaking is prevalent during fracture, whereas further away from this region the empirical potential description is adequate. The particular methodology chosen to model the immediate neighborhood of the crack tip, a semiempirical nonorthogonal TB scheme [91], describes well the bulk, amorphous, and surfaces properties of Si. Figure 5 shows the spatial decomposition of the computational cell into five different dynamic regions of the simulation: the continuum FE region at the far-field, where the atomic displacements and strain gradients are small; the atomistic MD region around the crack, with large strain gradients but with no bond breaking; the quantum mechanical region (labeled TB because of the use of the tight-binding method) right at the crack tip, where atomic bonds are being broken and formed; the FE/MD handshaking region; and the MD/TB handshaking region. The total Hamiltonian H_{tot} for the entire system was written as

$$H_{\text{tot}} = H_{\text{FE}}(\{\mathbf{u}, \dot{\mathbf{u}}\} \in \text{FE}) + H_{\text{MD}}(\{\mathbf{r}, \dot{\mathbf{r}}\} \in \text{MD}) + H_{\text{TB}}(\{\mathbf{r}, \dot{\mathbf{r}}\} \in \text{TB})$$

$$+ H_{\text{FE/MD}}(\{\mathbf{u}, \dot{\mathbf{u}}, \mathbf{r}, \dot{\mathbf{r}}\} \in \text{FE/MD}) + H_{\text{MD/TB}}(\{\mathbf{r}, \dot{\mathbf{r}} \in \text{MD/TB})$$

The degrees of freedom of the Hamiltonian are atomic positions $\mathbf{r}$ and velocities $\dot{\mathbf{r}}$ for the TB and MD regions and displacements $\mathbf{u}$ and their time rates of change $\dot{\mathbf{u}}$ for the FE regions. Equations of motion for all the relevant variables in the system are obtained by taking appropriate derivatives of this Hamiltonian. All variables can then be updated in lock-step as

Figure 5. Geometrical decomposition of a Si slab with a small crack into different dynamic regions in a macrosopic-atomistic–*ab initio* dynamics simulation: (a) The system at the macroscopic scale, which is modeled as a continuum using finite elements (FEs), except for the region near the crack, outlined in dashed line. (b) The mesoscopic scale, treated atomistically with interatomic potentials and molecular dynamics (MD), with the atoms indicated by green circles, except for the region in the immediate neighborhood of the crack, which is outlined in a dashed line. (c) The microcopic scale, treated atomistically with forces derived from quantum mechanical calculations, with the atoms indicated by red circles. The handshaking regions between FE and MD and between MD and tight binding (TB) are also shown schematically (see text for details).

a function of time using the same integrator. Thus, the entire time history of the system may be obtained numerically, given an appropriate set of initial conditions. Following trajectories dictated by this Hamiltonian leads to evolution of the system with conserved total energy, which ensures numerical stability.

The individual approaches at each level (FE, MD, and TB) are well-established and tested methods. What was much more important in this study was the seamless handshaking of the different methods at the interface of the respective domains; namely, the handshaking algorithms between the FE and MD regions and between the MD and TB regions. We present here the main ideas behind the coupling of the different regions.

3.1.1. FE/MD Coupling

To achieve the FE/MD handshaking, the FE mesh spacing is scaled down to atomic dimensions at the interface of the two regions. In Fig. 5, the FE nodes are indicated as small open circles connected by thin lines. Moving away from the FE/MD region and deep into the continuum, one can expand the mesh size. In this way, the atomistic simulation is embedded in a large continuum solid, indicated by a green-colored region in Fig. 5a. FE cells contributing fully to the overall Hamiltonian (unit weight) are marked with thin solid lines, whereas cells contributing to the handshake Hamiltonian (half weight) are represented by thin dashed lines. Interactions between the atoms on the MD side, which are represented by an interatomic potential, carry full weight when fully inside the MD region (thick solid lines joining neighboring atoms) and half weight (thick dashed lines) when they cross the boundary, with one of the neighbors effectively represented by a node in the FE region. The FE/MD interface is chosen to be far from the fracture region. Hence, the atoms of the MD region and the displacements of the FE lattice can be unambiguously mapped onto one another. The assignment of weights equal to unity within each region and equal to one-half at the interface is arbitrary and can be generalized by the introduction of a smooth step function.

3.1.2. MD/TB Coupling

At this interface, the atoms treated quantum mechanically are shown in red and those treated classically are shown in green. The dangling bonds at the edge of the TB region are terminated with pseudo-hydrogen atoms. The Hamiltonian matrix elements of these pseudo-hydrogen atoms are carefully constructed to tie off a single Si bond and to ensure the absence of any charge transfer when that atom is placed in a position commensurate with the Si lattice. In other words, the TB-terminating atoms are fictitious monovalent atoms forming covalent bonds with the strength and length of bulk Si bonds. These fictitious atoms are called "silogens": They behave mechanically just like Si, but chemically like H. The TB Hamiltonian including silicon–silicon and silicon–silogen matrix elements is then diagonalized to obtain electronic energies and wavefunctions, from which the total energy can be computed. Thus, at the perimeter of the MD/TB region, there are silogens sitting directly on top of the atoms of the MD region, which are shown as the smaller red circles on top of the green circles in Fig. 5. On one side of the TB/MD interface, the bonds to an atom are derived from the TB Hamiltonian, and are shown as shaded regions in Fig. 5, to indicate the electronic distribution responsible for the formation of the covalent bonds. On the other side of the interface, the bonds are derived from the interatomic potential of the MD simulation. The MD atoms of the interface have a full complement of neighbors, including neighbors whose positions are determined by the dynamics of atoms in the TB region; these are shown as small green circles on top of the red circles in Fig. 5. As before, the TB code updates atomic positions in lockstep with its FE and MD counterparts.

The MAAD approach was employed to study the brittle fracture of Si in a geometry containing a small crack (notch) within an otherwise perfect solid, with the exposed notch face in the (100) plane and the notch pointed in the $\langle 010 \rangle$ direction. The system consisted of 258,048 mesh points in each FE region, 1,032,192 atoms in the MD region, and approximately 280 unique atoms in the TB region (for computational reasons, the entire region modeled by the TB method was broken into smaller, partially overlapping regions, each assigned to a different processor in a parallel implementation). The lengths of the MD region are 10.9 Å for

the slab thickness along the front of the crack, 3649 Å in the primary direction of propagation, and 521 Å in the direction of pull (before pulling). Periodic boundary conditions were imposed at the slab faces normal to the direction of the crack propagation (along the front of the crack). The wall-clock time for a TB force update was 1.5 s, that for the MD update was 1.8 s, and that for the FE update was 0.7 s. The TB region was relocated after every 10 time steps to ensure that it remained at the very tip of the propagating crack. The computational slab was initialized at zero temperature, and a constant strain rate was imposed on the outermost FE boundaries defining the opposing horizontal faces of the slab. Furthermore, a linear velocity gradient was applied within the slab, which results in an increasing internal strain with time. It was observed that the Si solid failed in a brittle fashion at the notch tip when the material was stretched by ~1.5%. The limiting speed of crack propagation was found to be 85% of the Rayleigh speed with the chosen computational setup. In the course of the simulation, the straight-ahead brittle cleavage of the Si slab left behind a rough surface, with increased roughening as a function of crack distance. On the basis of these results, the authors suggested that the roughening surface is the result of the spawning of dislocations with low mobility on the timescale of the crack motion.

A general problem associated with domain decomposition, as in the MAAD simulations, is the spurious reflection of elastic waves (phonons) at the domain boundaries because of the changes in system description across the boundaries. For example, such effects have been observed in the atomistic modeling of dislocation motion [92], crack propagation [93–96], and energetic particle–solid collisions [97, 98], all of which involved some domain coupling scheme. Because the MAAD method involves domain decomposition into the TB, MD, and FE regions, the quality of coupling between different regions needs to be examined. In a subsequent paper, Broughton et al. reported that there was no visible reflection of phonons at the FE/MD interface and no obvious discontinuities at the MD/TB interface [26]. Thus, in this scheme the coupling between the various domains is indeed performed in a seamless manner, closely mimicking the actual behavior of the physical system under investigation. Overall, the MAAD approach represents state-of-the-art current multiscale simulation strategies. It is a finite-temperature, dynamic, and parallel algorithm that, at least as far as general computational aspects are concerned, is applicable to any type of material.

Ongoing efforts are exploring the possibility of applying the MAAD strategy to studying chemical effects on mechanical properties of metallic alloys, such as impurity effects on dislocation motion, crack nucleation, and propagation in various metals. There is an important qualitative difference between such systems and the study of the brittle fracture of Si mentioned above: The nature of bonds in metallic systems is very different from the simple covalent bonds in Si. This makes necessary the development of a different way of coupling the quantum mechanical to the classical atomistic region, because it is no longer feasible to terminate the bonds at the boundary of the quantum region by simply saturating them with fictitious atoms such as the silogens. In such endeavors, other more efficient and versatile quantum mechanical formulations are desirable. One candidate is the linear-scaling real space kinetic energy functional method [99]. This method approximates the noninteracting kinetic energy of DFT as a functional of electron density, and electronic wave-functions are thus eliminated from calculations; therefore, the method is termed as orbital-free density-functional theory (OFDFT). As a consequence, no diagonalization of the electronic Hamiltonian and no sampling of reciprocal space are necessary, making the method computationally efficient [100]. In particular, the explicit real space feature of this approach makes it naturally suitable for domain coupling within the MAAD framework. Although efforts to construct a fully functioning scheme along these lines are continuing, we believe this is a promising method with great potential for applications in metallic systems, which are difficult to handle with other techniques.

3.2. Quasicontinuum Model

One observation from many large-scale atomistic simulations is that only a small subset of atomic degrees of freedom do anything interesting. The great majority of the atoms behave in a way that could be described by effective continuum models like the elasticity theory.

The computation and storage of the uninteresting degrees of freedom—necessary for a fully atomistic calculation—consume a large proportion of computational resources. This observation calls for novel multiscale approaches that can reduce the number of degrees of freedom in atomic simulations [101, 102]. One such approach, proposed by Tadmor, Ortiz, and Phillips, is particularly promising and has yielded considerable success in many applications [103]. This concurrent multiscale approach is called the quasicontinuum method, and it seamlessly couples the atomistic and continuum realms. The chief objective of the approach is to systematically coarsen the atomistic description by the judicious introduction of kinematic constraints. These kinematic constraints are selected and designed so as to preserve full atomistic resolution where required—for example, in the vicinity of lattice defects—and to treat collectively large numbers of atoms in regions in which the deformation field varies slowly on the scale of the lattice. Variants of the quasicontinuum model have been developed and applied in different situations [103–114]. The essential building blocks of the static quasicontinuum model are the constrained minimization of the atomistic energy of the solid, the use of summation rules to compute the effective equilibrium equations, and the use of adaptation criteria to tailor the computational mesh to the structure of the deformation field. An extension of the method to finite temperature has also been proposed [115].

The quasicontinuum model starts from a conventional atomistic description, which computes the energy of the solid as a function of the atomic positions. (A web site with useful information related to the quasicontinuum method can be found at http://www.qcmethod.com, where the quasicontinuum codes are also available to download.) The configuration space of the solid is then reduced to a subset of representative atoms. The positions of the remaining atoms are obtained by piecewise linear interpolations of the representative atom coordinates, much in the same manner as displacement fields are constructed in the FE method. The effective equilibrium equations are then obtained by minimizing the potential energy of the solid over the reduced configuration space. A direct calculation of the total energy in principle requires the evaluation of sums that are extended over the full collection of atoms; namely

$$E_{\text{tot}} = \sum_{i=1}^{N} E_i \tag{14}$$

where N is the total number of atoms in the solid. The full sums may be avoided by the introduction of approximate summation rules. For example, the lattice quadrature analog of Eq. (14) can be written as

$$E_{\text{tot}} \approx \sum_{i=1}^{N_r} n_i \overline{E}_i \tag{15}$$

where n_i is the quadrature weight that signifies how many atoms a given representative atom stands for in the description of the total energy and $\overline{E}_i$ is the energy of ith representative atom. Note that in this case the sum is over the N_r representative atoms only. In the quasicontinuum approach, the FE method serves as the numerical tool for determining the displacement fields, whereas an atomistic calculation is used to determine the energy of a given displacement field. The positions of the coarse-grained atoms are needed because the energy of the representative atoms depends on them. This approach is in contrast to standard FE schemes, in which the constitutive law is introduced through a phenomenological model. The selection of the representative atoms may be based on the local variation of the deformation field. For example, near dislocation cores and on planes undergoing slip, full atomistic resolution is attained with adapted meshing. Far from defects or other highly stressed regions, the density of representative atoms rapidly decreases, and the collective motion of very large numbers of atoms is dictated without appreciable loss of accuracy by a small number of representative atoms.

The quasicontinuum method has been applied to a variety of problems, including dislocation structures [103, 104], interactions of cracks with grain boundaries [105], nanoindentations [110, 112, 114], dislocation junctions [108], atomistic-scale fracture process [106],

and so forth. By way of example, Shenoy et al. applied the method to study the interaction of dislocations with grain boundaries (GBs) in Al [105]. In particular, they considered a reformulation of the quasicontinuum model that allows for the treatment of interfaces, and therefore of polycrystalline solids. As the first test of the model, they computed the GB energy and atomic structure for various symmetric tilt GBs in Au, Al, and Cu, using both direct atomistic calculations and the model calculations. They found excellent agreement between the two sets of calculations, indicating the reliability of the model for their purpose. In the study of Al, they used nanoindentation-induced dislocations to probe the interaction between dislocations and GBs. Specifically, they considered a block oriented so that the (111) planes are positioned to allow for the emergence of dislocations, which then travel to the Σ 21($\bar{2}$41) GB located at ~200 Å beneath the surface (see Fig. 6a). First, the energy minimization is performed to obtain the equilibrium configuration of the GB, then a mesh is constructed accordingly, as shown in Fig. 6a. The region that is expected to participate in the dislocation–GB interaction is meshed with full atomistic resolution, whereas in the far fields the mesh is coarser. The displacement boundary conditions at the indentation surface are then imposed onto this model structure, and after the critical displacement level is reached, dislocations are nucleated at the surface. With the EAM potential [12] supplying the atomistic energies in the quasicontinuum approach, the authors observed closely spaced (15 Å) Shockley partials nucleated at the free surface. As seen from Fig. 6b, the partials are subsequently absorbed at the GB with the creation of a step at the GB, and no evidence of slip transmission into the adjacent grain is observed. The resultant structure can be understood based on the concept of the displacement shift complete lattice [116] associated with this symmetric-tilt GB. As the load is increased, the second pair of Shockley partials is nucleated. These partials are not immediately absorbed into the GB, but instead form a pile-up (Fig. 6b). The dislocations are not absorbed until a much higher load level is reached. Even after the second set of partial dislocations is absorbed at the GB, there is no evidence of slip transmission into the adjacent grain, although the GB becomes much less ordered. The authors argued that their results give hints for the general mechanism governing the absorption and transmission of dislocations at GBs. The same work also studied the interaction between a brittle crack and a GB and observed stress-induced GB motion (the combination of GB sliding and migration). In this example, the reduction in the computational effort associated with the quasicontinuum thinning of degrees of freedom is significant. For example, the number of degrees of freedom associated with the mesh of Fig. 6a is about 10^4, three orders of magnitude smaller than what would be required by a full atomistic simulation (10^7 degrees of freedom).
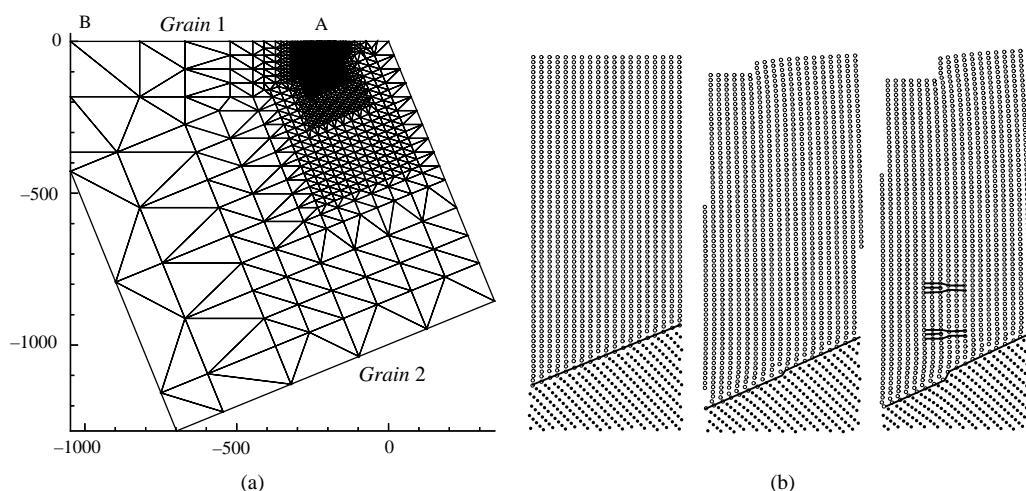
Figure 6. Example of a multiscale simulation using the quasicontinuum method. (a) Finite-element mesh used to model dislocation-grain boundary interaction. The surface marked AB is rigidly indented to generate dislocations at A (distance in Amstroms). (b) Snapshots of atomic positions at different stages in the deformation history. Absorption of the first pair of dislocations at the GB results in a step, while the second pair form a pileup.

Recently, the quasicontinuum model has been extended to complex Bravais lattices [117], whereby more complicated materials can be handled [114]. However, because of the expression for the total energy adopted in Eqs. (14) and (15), the actual atomistic methods that can be implemented in the quasicontinuum model are limited to ones that can be easily cast in such a form, if one insists on having the ability to resolve the FE nodes all the way to the atomic scale. This limit is often referred to in the literature as the "nonlocal" regime of the quasicontinuum method. In contrast, the "local" limit refers to the case in which each FE node represents a very large number of atomistic degrees of freedom, which is modeled as corresponding to an infinite solid homogeneously deformed according to the local strain at the node. In this limit, it is advantageous to employ effective Hamiltonians to compute energetics for the representative atoms. Such Hamiltonians can be constructed from *ab initio* calculations and may include physics that atomistic simulations based on classical interatomic potentials (such as EAM) are not able to capture. For example, by constructing an effective Hamiltonian parametrized from *ab initio* calculations, Tadmor et al. were able to study polarization switching in piezoelectric material $PbTiO_3$ in the context of the quasicontinuum model in the local limit [118]. This particular Hamiltonian includes the following terms: the elastic energy of the lattice, the coupling between strain and atomic displacement, harmonic and anharmonic phonon energy contributions, the interaction of atomic displacement with the applied electric field, and the electrostatic energy. With this effective Hamiltonian, it was shown that the behavior of a large-strain ferroelectric actuator under the application of competing external stress and electric fields can be modeled successfully, reproducing, for example, all the important features of the experimental strain versus the electric field curve for the actuator. The advantage of these simulations is that they also provide insight into the microscopic mechanisms responsible for the macroscopic behavior, making possible the improvement of design of the technologically useful materials.

One pitfall of the quasicontinuum model is the so-called "ghost force" at the interface between the local region, identified with slow variation of the deformation gradient, and the nonlocal region, identified with rapid variation of the deformation gradient [109]. The error arises from the fact that different energy formulations are used for local and nonlocal regions, and Newton's third law is not satisfied across the local–nonlocal interfaces. Care must be taken to correct these "ghost forces" [109]. Finally, we should point out that the quasicontinuum approach also shares certain features with sequential approaches; namely, the constitutive equation for the FE nodes is drawn from atomistic calculations (akin to message-passing in sequential approaches). The reason we categorize it as a concurrent multiscale approach is that the atomistic and FE calculations are performed concurrently rather than in sequence, as the range of deformations encountered in various parts of the system are not known beforehand. Moreover, some sort of domain partitioning (meshing) is involved in the quasicontinuum approach.

3.3. Coarse-grained Molecular Dynamics

Mesoscopic elastic systems, and in particular nano-electro-mechanical systems (NEMS), recently have captured a great deal of attention and research interest as nanoscale machines and devices. However, there is serious concern regarding their mechanical integrity and stability in applications because these nanoscale devices are so minuscule that structural defects and surface effects could have a large effect on their performance. However, the computational study of the mechanical properties of the NEMS has turned out to be extremely difficult because they are too small in size for FE simulations (at the limit at which continuum elasticity theory may be no longer valid), but too large for atomistic simulations. To resolve this problem, a concurrent multiscale simulation strategy called coarse-grained molecular dynamics (CGMD) has been developed by Rudd and Broughton [119, 120]. This approach bears some resemblance to the quasicontinuum model, yet there exist important differences between the two.

The CGMD approach is based on a statistical coarse-graining prescription. In particular, the model aims at constructing scale-dependent constitutive equations for different regions in a material. In general, the material of interest can be partitioned into cells, whose size varies

so that in important regions a mesh node is assigned to each equilibrium atomic position, whereas in other regions the cells contain many atoms, and the nodes need not coincide with atomic sites. The CGMD approach produces equations of motion for a mean displacement field defined at the nodes by defining a conserved energy functional for the coarse-grained system as a constrained ensemble average of the atomistic energy under fixed thermodynamic conditions. The key point of this effective model is that the equations of motion for the nodal (mean) fields are not derived from the continuum model but from the underlying atomistic model. The nodal fields represent the average properties of the corresponding atoms, and equations of motion (in this particular case Hamilton's equations) are constructed to describe the mean behavior of underlying atoms that have been integrated out.

One important underlying principle of CGMD is that the classical ensemble must obey the constraint that the position and momenta of atoms are consistent with the mean displacement and momentum fields. To be specific, let the displacement of atom μ be $\mathbf{u}_\mu = \mathbf{x}_\mu - \mathbf{x}_{\mu 0}$, where $\mathbf{x}_{\mu 0}$ is its equilibrium position. The displacement of mesh node j is an average of the atomic displacements

$$\mathbf{u_j} = \sum_\mu f_{j\mu} \mathbf{u}_\mu \tag{16}$$

where $f_{j\mu}$ is a weighting function, a microscopic analog of the FE interpolating functions. Note that Latin indices j and k denote mesh nodes and the Greek indices μ and ν denote atoms. A similar relation holds for the momenta $\mathbf{p}_\mu$. Because the nodal displacements are fewer or equal to the atomic positions in number, fixing the nodal displacements and momenta does not necessarily entirely determine the atomic positions. Therefore, some subspace of phase space remains not sampled, which corresponds to the degrees of freedom that are missing from the mesh points. The coarse-grained energy is defined as the average energy of the canonical ensemble on this constrained phase space

$$E(\mathbf{u}_k, \dot{\mathbf{u}}_k) = \langle H_{MD} \rangle_{\mathbf{u}_k, \dot{\mathbf{u}}_k}$$

$$= \int d\mathbf{x}_\mu d\mathbf{p}_\mu H_{MD} e^{-\beta H_{MD}} \Delta / Z,$$

$$\Delta = \prod_j \delta \left(\mathbf{u}_j - \sum_\mu \mathbf{u}_\mu f_{j\mu} \right) \delta \left(\dot{\mathbf{u}}_j - \sum_\mu \frac{\mathbf{p}_\mu f_{j\mu}}{m_\mu} \right) \tag{17}$$

where $\beta = 1/(k_B T)$ is the inverse temperature and Z is the partition function. The three-dimensional delta functions $\delta(\mathbf{u})$ enforce the mean field constraint [Eq. (16)].

When the mesh nodes and the atomic sites are identical, the CGMD equations of motion agree with the atomistic equations of motion. As the mesh size increases, some short-wavelength degrees of freedom are not supported by the coarse mesh, but these degrees of freedom are not neglected entirely, because their thermodynamic average effect has been retained. This approximation is expected to be good if the system is initially in thermal equilibrium and the missing degrees of freedom only produce adiabatic changes to the system. The Hamiltonian was derived originally for a monoatomic harmonic solid but can be easily generalized to polyatomic solids [119]. After deriving the equations of motion from the assumed Hamiltonian for a particular system, one can perform the CGMD for the nodal points.

As proof of principle, the method was applied to one-dimensional chains of atoms with periodic boundary conditions, where it was shown that the CGMD gives better results for the phonon spectrum of the model system compared to two different FE methods [119]. A variety of other calculations have also been performed with the CGMD to validate its effectiveness [120, 121].

Although the CGMD has proven to be reliable in the description of lattice statics and dynamics, the implementation of the model varies from system to system. This is because different approximations have to be made to the Hamiltonian that represents a particular system. However, such approximations can be estimated and controlled in the CGMD method. This advantage makes the CGMD method a good candidate for replacing the FE method

in the MAAD approach when a high quality of FE/MD coupling is required. As we alluded earlier, the CGMD approach resembles the quasicontinuum model in the sense that both approaches adopt an effective field model, an idea rooted in the renormalization group theory for critical phenomena. In both approaches, less important (long-wavelength) degrees of freedom are removed while the effective Hamiltonian is derived from the underlying fine-scale (atomistic) model. Although both approaches are developed to couple FE and atomistic models, the quasicontinuum method is mainly applicable to zero-temperature calculations, whereas the CGMD is designed for finite-temperature dynamics. The quasicontinuum model has shown its success in many applications, but the CGMD approach has yet to show its wider applicability and versatility.

3.4. Other Works

Recently, a more general model for the dynamics of coarse-grained multiscale systems was proposed by Curtarolo and Ceder [122]. The model is similar to the Migdal–Kadanoff approach in the renormalization group theory [123], in which the system is coarse-grained through a bond-moving process. The new potentials are constructed to ensure that the partial partition function of the system remains unchanged. The information removed from the coarse-graining process can be quantified by the entropy contribution of each step. Although the model is shown to produce excellent results for mechanical and thermodynamical properties compared to the non-coarse-grained system, so far it is limited to two-dimensional systems, and its generalization to three dimensions is yet to be achieved and tested.

Another interesting approach has been developed by Shilkrot, Miller, and Curtin, aimed at linking an atomistic region to a "defected" dislocation dynamics region [124]. In this coupled atomistic and discrete dislocation (CADD) method, the fully atomistic region is directly coupled to a linear elastic continuum region containing dislocations that are modeled as continuum elastic line defects. The dislocations at the continuum region are treated with the standard discrete dislocation method [125], and the atomistic region may have any kind of atomic scale defects. The key aspect of the CADD method is that the dislocations can pass between the atomistic and continuum regions smoothly. Two developments have been made to achieve this goal: first, the detection of the dislocation near the atomic–continuum interface, and second, a procedure for moving the "right" dislocations across the interface. So far, this approach has only been implemented in two-dimensional systems, but it has been shown to agree quite well with the two-dimensional atomistic calculations for Al.

Some other concurrent approaches are similar to the MAAD method but concentrate on linking two different length scales rather than three. For example, Bernstein and Hess [126] have simulated brittle fracture of Si by dynamically coupling empirical-potential MD and semiclassical TB approaches. In a similar vein, Lidorikis et al. have studied stress distribution in Si/Si_3N_4, using a hybrid MD and FE approach [127]. More recently, a first-principles Green's function boundary condition method has been developed to self-consistently couple the strain field produced by a line defect to the long-range elastic field of the host lattice [128].

Concurrent multiscale ideas have also been applied to the modeling of polymers [129] and biomolecules. In particular, the hybrid quantum mechanical and molecular mechanical (QM/MM) methods have been gaining ground in the study of proteins and enzymes in which the small part of a molecule (active site) is modeled by *ab initio* methods while the rest of the molecule can be dealt with by a more approximate classical force field theory [130]. One particular implementation [131] of the QM/MM strategy is to combine the quantum mechanical self-consistent-charge density-functional-based TB method [132] with the CHARMM molecular force fields [133]. This approach has been used to study the reactions catalyzed by triosephosphate isomerase and the dynamics of small peptide helices in water [131].

Finally, we wish to comment that many concurrent models such as the ones discussed above are designed for covalently bonded systems. These methods take advantage of the localized electron bonding across the domain interface (between TB/MD and between QM/MM) and partition the bonding energy approximately, with a certain degree of empiricism. For metallic systems, however, the bonds are not localized or associated with a distinct pair of atoms; therefore, the concept of "bonding energy partition" across the domain

interface becomes invalid, and new concepts are needed. Recently, several groups have exploited the idea of "embedding potential" in simulations in which a region (I) with a more accurate description of the physics is embedded into another region (II) with a less accurate description. The influence of region II on region I is described by the "embedding potential," which corresponds to a local one-electron operator in the framework of the DFT [134–137]. For example, in an effort to improve the LDA/DFT description of molecular adsorption on surfaces, a coupling method was developed in which a more accurate (quantum chemical) region (I) was embedded in a less accurate LDA/DFT region (II) [134, 135, 137]. The "embedding potential" is defined as the functional derivative of the coupling energy with respect to the electron density $\rho_I(\mathbf{r})$ in region I. The total electron density $\rho_{\text{tot}} = \rho_I + \rho_{II}$, where ρ_{II} is the electron density in the LDA/DFT region, can be obtained by just LDA/DFT calculations for the entire system because the electron density is usually well represented by LDA/DFT. ρ_{tot} is then held fixed during the subsequent calculations. By employing the OFDFT method [100] for the coupling energy, the "embedding potential" can be explicitly evaluated for any given $\rho_I(\mathbf{r})$. The "embedding potential" as an effective local one-electron operator can in turn be added to the Hamiltonian of region I, and the new electron density $\rho_I(\mathbf{r})$ is thus determined. In this way, $\rho_I(\mathbf{r})$ can be updated self-consistently for the given ρ_{tot}. The same "embedding potential" idea can be applied to the coupling between two different DFT regions, or between two regions, where one is treated with DFT, and the other is treated classically, for instance, with EAM.

This last approach, currently under development in our group, deserves some elaboration. This approach strives to combine quantum mechanics via OFDFT, classical mechanics via EAM, and continuum mechanics via the quasicontinuum method in a unified description for metallic systems. Because the electron density defined in the EAM potential along with the EAM nuclei could generate an "embedded potential" that the OFDFT electrons experience, the coupling energy between OFDFT and EAM regions can be explicitly calculated. Furthermore, the EAM atomistic region can be easily coupled to the continuum region based on the nonlocal description of the quasicontinuum framework.

4. EXTENDING TIMESCALES

4.1. Accelerated Dynamics

As we have seen, MD plays a critical role in the modeling of materials problems because MD simulations can follow the actual dynamical evolution of the system without assuming any mechanism or pathway for the dynamics, in contrast to, say, Monte Carlo or molecular statics simulations. However, MD is typically limited to a timescale of nanoseconds because standard MD simulations follow the individual vibrations of all the atoms, whose vibration frequencies are on the order of 10^{14} s^{-1}. This is particularly troublesome for the complex systems whose dynamics are characterized by the occurrence of rare but important events, such as chemical reactions, diffusion processes, and conformational changes. In these systems, the existence of energetic barriers much larger than $k_B T$ that separate the initial from the final state leads to reaction times far greater than those that can be currently accessed computationally. The other reason for extending timescales is that time is a sequential object, and the current progress in parallel computing has little effect on solving the problem. Therefore, algorithms that could address the timescale problem could revolutionize the field of computational materials science and engineering.

In the past few years, significant progress has been made in accelerating MD simulations. A class of accelerated dynamics methods, including hyperdynamics, parallel replica dynamics, and temperature-accelerated dynamics, has been developed by Voter and coworkers [138–140]. Although each method accomplishes this acceleration in a different way, transition-state theory (TST) provides the common theoretical foundation. TST is an elegant theory with extensive applications in materials science [141–146]. In TST theory, a state-to-state transition rate constant (K^{TST}) is approximated as the flux through a dividing surface in the phase space separating the initial and final states. A common and useful approximation to TST is the harmonic TST, in which one assumes that the potential energy surface (PES)

near the minimum can be expanded with the harmonic approximation. Thus, the TST rate constant (the flux through the saddle plane) becomes

$$K^{HTST} = \nu_0 \exp(-E/k_B T) \tag{18}$$

where

$$\nu_0 = \frac{\prod_i^{3N} \nu_i}{\prod_i^{3N-1} \nu_i'} \tag{19}$$

Here E is the activation energy (energy difference between the minimum and the saddle point), ν_i is the ith normal mode frequency at the minimum, and ν_i' is the nonimaginary normal model frequency at the saddle point [146]. The analytic integration over the whole phase space yields the well-known Arrhenius temperature dependence. It is worthwhile pointing out that although the exponent depends only on the barrier height, there is no assumption that the trajectory passes exactly through the saddle point. For systems in which there is no recrossing of the dividing surface and the modes are truly harmonic, the rate [Eq. (18)] is exact. The underlying concept in the accelerated dynamics methods is that the system trajectory is simulated to find an appropriate pathway for escape from an energy well by a process that takes place much faster in the simulation than it would with direct MD. We provide below an elementary description of this concept.

The general formulation of TST rests on two assumptions to treat infrequent events: first, it is known in advance what the different equilibrium states of the system will be, and second, it is possible to construct a reasonable dividing surface along the boundaries between initial and final states (or, equivalently, all the saddle points can be identified). Unfortunately, the knowledge of states through which a system may evolve in most cases (especially in complex systems) is incomplete. The hyperdynamics method [139, 140] is designed to accelerate MD simulations without any advance knowledge of either the location of the dividing surface or the states through which the system may evolve. Based on TST, Voter has shown that it is possible to modify the PES of the system in such a way that a simulation on this modified surface exhibits the correct relative probabilities of transitions, but with enhanced overall transition rates for the system escaping from one equilibrium state to the various nearby equilibrium states. The key of this approach is to construct a bias potential to raise the energy of the system in regions other than at the dividing surfaces. Dynamical evolution with the biased potential leads to accelerated transition from one equilibrium state to another equilibrium state, whereas the elapsed time is related to statistical properties of the system. More precisely, the total time advance for a hyperdynamics simulation after n integration steps is

$$t_{\text{hyper}} = \sum_{j=1}^{n} \Delta t_{\text{MD}} e^{\Delta V(\mathbf{r}(t_j))/k_B T} \tag{20}$$

where Δt_{MD} is the time advance for a regular MD trajectory, $\Delta V(\mathbf{r})$ is the bias potential, and T is the temperature. The overall computational speed-up is given by the average boost factor ($t_{\text{hyper}}/t_{\text{MD}}$) divided by the extra computational cost of calculating the bias potential and its derivatives. The evolution of hyperdynamics from state to state is correct because the bias potential does not change the relative TST rates for different escape paths from a given state. The long-time dynamics of the simulations are exact to the extent that the dynamical corrections to the TST are negligible. Recently, Voter has shown that the bias potential and its derivatives can be computed in $O(N)$ fashion without ever constructing the Hessian [140]. Thus, the implementation of the hyperdynamics method requires only first derivatives of the interatomic potential, as for normal MD simulations.

To demonstrate the effectiveness of the method, Voter has studied the diffusion of an Ag adatom on the Ag (100) surface at 400 K using an EAM potential for the energetics. He found that a 3.7×10^6 steps of hyperdynamics run gave an average boost of 1356, for a total time of 9.89 ± 0.5 μs. Each hyperdynamics step required $\sim$30 times the computational time of a direct MD step; therefore, the net computational boost was a factor of 45. The rate constants obtained from the calculations are in agreement with the full harmonic rate.

For a more complex system with a 10-atom Ag cluster on the Ag (111) surface at 300 K, he achieved an average boost of 8310 with a hyperdynamics run for 221.2 μs. With this approach, one should be able to observe novel diffusion mechanisms that can not be accessed by normal MD simulations.

To take advantage of recent advances in parallel computation, Voter proposed the so-called parallel replica dynamics method [147] to treat infrequent events. For a system in which successive transitions are uncorrelated, running a number of independent MD trajectories in parallel gives the exact dynamical evolution between the states. For a system with correlated crossing events, the state-to-state transition sequence is still correct, but care must be taken to eliminate or reduce the error associated with the simulation time. The parallel replica method represents the simplest and most accurate of the accelerated dynamics techniques, with the only assumption being that of infrequent events obeying first-order kinetics. To be more specific, the probability distribution for the waiting time before the next escape is assumed to be

$$p(t) = K \exp(-Kt) \tag{21}$$

where K is the rate constant for finding the next escape path from the current state. In a system that exhibits no correlated crossing events, K is exactly the TST rate constant (K^{TST}). In a more general case, in which correlated crossings occur, $K < K^{TST}$. For an N-atom system in a particular equilibrium state (potential energy basin), the entire system is replicated on each of M available parallel or distributed processors. After a short dephasing stage, during which momenta are periodically randomized to eliminate correlations between replicas, each processor carries out an independent constant-temperature MD trajectory for the entire N-atom system, thus exploring the phase space within the particular basin M times faster than a single trajectory would. Whenever a transition is detected on any processor, all processors are alerted to stop. The simulation clock is advanced by the accumulated trajectory time summed over all replicas (i.e., the total time spent exploring phase space within the basin before the escape pathway is found). The parallel replica method also correctly accounts for correlated dynamical events in which TST is no longer valid. This is accomplished by allowing the trajectory that made the transition to continue on its processor for a further amount of time Δt_{corr}, during which recrossings or follow-on events may occur. The simulation clock is then advanced by Δt_{corr}, the final state is replicated on all processors, and the whole process is restarted. This overall procedure then gives exact state-to-state dynamical evolution because the escape times obey the correct probability distribution [138]. With this approach, significant extensions of MD timescales can be achieved. For example, in MD simulations of vacancy diffusion on the Cu(100) surface at 500 K, a 15-processor parallel computer can give a 14-fold increase in simulation time per wall-clock time. Moreover, the parallel replica method can be combined with other accelerated dynamics methods, such as hyperdynamics, to give a multiplicative effect in the MD timescale gain [147].

In the temperature-accelerated dynamics (TAD) method, the transition from state to state is accelerated by the increasing temperature [148]. The transitions that should not have occurred at the original temperature are then filtered out. The TAD method is more approximate than the previous two methods because it relies on the harmonic TST approximation, but it often gives substantially bigger boost than the hyperdynamics or the parallel replica dynamics in systems in which the approximation is justified. Consistent with the accelerated dynamics concept, the trajectory in TAD is allowed to wander on its own to find each escape path, so that no prior information is required about the nature of the reaction mechanisms [138]. Like hyperdynamics, TAD can also be combined with the parallel replica method to achieve an even higher acceleration on parallel computers.

4.2. Finding Transition Pathways

As stated earlier, the problem of finding transition pathways for infrequent events between two known equilibrium (stable or metastable) states is of considerable interest. The accelerated dynamics methods are designed to find the real dynamic pathways via effective MD simulations. Other methods requiring no preconceived mechanism or transition state have

also been developed to locate transition pathways. For example, Elber and Karplus [149] developed a method to find the transition pathway by minimizing the average value of the potential energy along the path rather than trying to find the path with the lowest barrier. A more popular approach, similar in spirit to the Elber–Karplus method, is the so-called nudged elastic band (NEB) approach [150, 151], which focuses on the global character of the path rather than on local properties of the PES.

The NEB method is based on the "chain-of-states" idea, where a number of images (or replicas or "states") of the system are connected together between the endpoint configurations to trace out a transition pathway [150]. If the images are connected with springs of zero natural length, one can define the object function for the so-called plain elastic band (PEB) method in the following

$$S^{\text{PEB}}(\vec{R}_1, \ldots, \vec{R}_{P-1}) = \sum_{i=0}^{P} \mathcal{V}(\vec{R}_i) + \sum_{i=1}^{P} \frac{Pk}{2}(\vec{R}_i - \vec{R}_{i-1})^2 \tag{22}$$

where vector $\vec{R}$ represents the coordinate of the system, $\mathcal{V}$ is the potential energy of the system, and k is the spring constant. The spring is introduced to ensure that the images are evenly spaced along the path. One would envision finding the transition pathway by minimizing the object function in Eq. (22) with respect to the intermediate images while keeping the endpoint images $\vec{R}_0$ and $\vec{R}_P$ fixed. The force acting on the image i is

$$\vec{F}_i = -\nabla \mathcal{V}(\vec{R}_i) + \vec{F}_i^s \tag{23}$$

where

$$\vec{F}_i^s = k_{i+1}(\vec{R}_{i+1} - \vec{R}_i) - k_i(\vec{R}_i - \vec{R}_{i-1}) \tag{24}$$

However, as demonstrated by Jónsson et al., the PEB method fails to provide the transition pathway in most situations [150]. For example, if k_i is too large, the elastic band becomes too stiff, and the transition path would then "cut the corner" and thus miss the saddle point region. In contrast, if k_i is small, the elastic band comes closer to the saddle point, but the images slide down from the energy barrier (and avoid the saddle point), therefore reducing the resolution of the path in the most critical region. Furthermore, by noticing the analogy between the object function in the continuum limit and the action of a classical particle of unit mass moving on the inverted PES, Jónsson et al. argued that the particle would move through the saddle point region with a finite velocity affected by the force component perpendicular to the curved path. In other words, the images would deviate from the minimum energy path (MEP). The problem with "corner cutting" is caused by the component of the spring force that is perpendicular to the path, which tends to pull images off the MEP. The problem with sliding down results from the component of the potential force or of the true force, $\nabla \mathcal{V}(\vec{R}_i)$ that is parallel to the path. The distance between images becomes uneven, so that the net spring force can balance the parallel component of the true potential force. To cure these problems, the NEB method projects out the perpendicular component of the spring force and the parallel component of the potential force relative to the path. The force on image i becomes

$$\vec{F}_i^0 = -\nabla \mathcal{V}(\vec{R}_i)|_\perp + \vec{F}_i^s \cdot \hat{\tau}_\parallel \hat{\tau}_\parallel \tag{25}$$

where $\hat{\tau}_\parallel$ is the unit tangent to the transition path and $\nabla \mathcal{V}(\vec{R}_i)|_\perp = \nabla \mathcal{V}(\vec{R}_i) - \nabla \mathcal{V}(\vec{R}_i) \cdot \hat{\tau}_\parallel \hat{\tau}_\parallel$. These force projections ("nudging") decouple the dynamics of the path itself from the discrete representation of the path. The spring force thus does not interfere with the relaxation of the images perpendicular to the path, and the relaxed configuration of the images satisfies $\nabla \mathcal{V}(\vec{R}_i)|_\perp = 0$ (i.e., they lie on the MEP).

The implementation of the NEB in a MD program is quite simple. First, the energy and its gradient are evaluated for each image in the elastic band, using some description of the energetics (*ab initio* or empirical force fields). Then, for each image, the local tangent to the path is estimated and the force defined in Eq. (25) is evaluated for an initial guess of the path.

The subsequent minimization for the magnitude of the forces with respect to the coordinates of the intermediate images can be carried out with the velocity Verlet algorithm [152]. Recently, several improvements of the original NEB have been proposed [151, 153, 154]. The NEB method has found a wide range of applications in materials problems, including a cross-slip of screw dislocations in metals [155], diffusion and atomic exchange processes at metal and semiconductor surfaces [156, 157], dissociative adsorption of molecules on surfaces [158], and contact formation of metal tips on surface [159]. The NEB method has been implemented in many empirical potential and *ab initio* atomistic approaches [150, 151]. One drawback of the NEB method is the difficulty in choosing appropriate spring constants. A large spring constant requires a small time step in the evolution of states (i.e., more images along the path). A small spring constant, however, may fail to achieve the desired uniformity of the images along the path and, hence, may reduce the accuracy for the energy barrier. Furthermore, like other methods in this category, the NEB method becomes less efficient or even inapplicable to systems with very rough energy landscapes.

Realizing the importance of real dynamical pathways, Chandler and collaborators have recently proposed methods for statistically sampling dynamical paths (MC sampling of MD trajectories) that do not require the assumption of TST or the existence of a single, well-defined transition state or transition path [160, 161]. In particular, no reaction coordinate is needed to study the dynamics or kinetics of rare transitions [162] with these methods. In a sense, the transition path-sampling methods are metaphorically akin to throwing ropes over rough mountain passes in the dark: "throwing ropes" corresponds to shooting short real dynamical trajectories, and "in the dark" implies that the high-dimensional systems are so complex that it is generally impossible to visualize the topography of relevant energy surfaces. Although these methods are extremely powerful for treating complex systems with rough energy landscapes, they are usually computationally demanding. In particular, their efficiency usually hinges on the ability to produce new accepted paths from old ones; thus, they have found limited application so far.

Recently, an alternative finite temperature string method was proposed that represents transition paths by their intrinsic parameterization to efficiently evolve and sample paths in the path space [163]. The string method performs a constrained sampling of the equilibrium distribution of the system in hyperplanes normal to the transition pathways of a coarse-grained potential that need not be determined beforehand. The collection of the hyperplanes is parametrized by a string that is updated self-consistently until it approximates locally the correct coordinate associated with the reaction event. The region in these planes in which the equilibrium distribution is concentrated determines a transition tube in the configuration space in which a transition takes place with high probability. The string method naturally overcomes the spring constant problem in the NEB method because of the intrinsic param-eterization of the string, and the distribution of the replicas along the chain is automatically uniform. The method, however, rests on the assumption that the equilibrium distribution must be localized on the iso-surfaces of the reaction coordinate and that these iso-surfaces can be locally approximated by the hyperplanes. If the effective transition tube is highly curved in configuration space, this approach may have to be modified.

A method for efficiently generating classical trajectories with fixed initial and final boundary conditions has recently attracted attention because of its conceptual and computational simplicity [164]. The approach developed by Passerone and Parrinello addresses a very general problem: Given an initial and a final configuration, what are the dynamical paths that connect them? Given a classical dynamical system described by a set of coordinates $\mathbf{q}$, its trajectory $\mathbf{q}(t)$ with boundary conditions $\mathbf{q}(0) = \mathbf{q}_A$ and $\mathbf{q}(\tau) = \mathbf{q}_B$ is determined by locating the stationary point of the action $\mathscr{S}$

$$\mathscr{S} = \int_0^\tau \mathscr{L}(\mathbf{q}(t), \dot{\mathbf{q}}(t)) \, dt, \tag{26}$$

where $\mathscr{L}$ is the Lagrangian $\mathscr{L} = \mathscr{T} - \mathscr{V}$ and $\mathscr{T}$ and $\mathscr{V}$ are the kinetic and potential energy, respectively. Following the work of Gillilan and Wilson [165], the action $\mathscr{S}$ can be

discretized as

$$\mathscr{S} = \sum_{j=0}^{N-1} \Delta \left[\frac{1}{2} \left(\frac{\mathbf{q_j} - \mathbf{q_{j+1}}}{\Delta} \right)^2 - \mathscr{V}(\mathbf{q_j}) \right] \tag{27}$$

where $\mathbf{q}_0 = \mathbf{q}_A$, $\mathbf{q}_N = \mathbf{q}_B$; $\Delta = \tau/N$ is the time interval and the mass is taken as unitary [164]. The stationary solution of this action is the discretized Euler–Lagrangian equation, and the corresponding trajectory is identical to the well-known Verlet trajectory. The novel part of this method is supplementing the action with a penalty function that favors the energy-conserving trajectories

$$\Theta(\mathbf{q}_j, E) = \mathscr{S} + \mu \sum_{j=0}^{N-1} (E_j - E)^2 \tag{28}$$

Here μ determines the strength with which the energy conservation is enforced, E_j is the instantaneous energy given by

$$E_j = (\mathbf{q}_j - \mathbf{q}_{j+1})^2/(2\Delta^2) + \mathscr{V}(\mathbf{q}_j)$$

and E is its target value. This is motivated by the fact that the physical trajectories have to conserve total energy. In all the systems studied, it was found that there exists a rather large interval of μ values such that Θ has a minimum close to the Verlet trajectories. To minimize the Θ function more efficiently, Passerone et al. make the transformation

$$\mathbf{q}_j = \mathbf{q}_A + \frac{j\Delta}{\tau}(\mathbf{q}_B - \mathbf{q}_A) + \sum_{i=1}^{N} \mathbf{a}_i \sin\left(\pi i \frac{j\Delta}{\tau} \right) \tag{29}$$

thus automatically satisfying the boundary conditions. The advantage of using $\mathbf{a}_i$ over $\mathbf{q}_j$ is that $\mathbf{a}_i$ has a global character. In practice, Θ is first optimized with respect to a relatively small number of $\mathbf{a}_i$, thus capturing the global features of the trajectory, and then higher frequency terms are added. Each time, a standard conjugate gradient algorithm is used to minimize Θ with only the evaluation of the forces. The computational scaling is therefore linear in the number of degrees of freedom, rather than quadratic, as in other approaches involving the Hessian matrix.

   To illustrate the performance of the method, Passerone et al. studied a few simple systems. For a one-dimensional double-well potential, they found that their solutions agree very well with the Verlet trajectory, but without the calculation of the Hessian matrix. The second example was a minimization of a trajectory in a two-dimensional configurational space; namely, in the Mueller potential [166]. Again, the authors found a satisfactory result; namely, that the trajectories pass exactly through the saddle point and that the overall behavior of the trajectories is physical. The last example was to look at a process in which the central atom of a seven-atom, two-dimensional Lennard–Jones cluster migrates to the surface. In this case, Passerone et al. claim that their calculations reproduce the results from the more elaborate method, which involves transition path-sampling procedure [167]. Finally, the authors pointed out that their method can be easily implemented within the Car–Parrinello MD approach [168], offering a powerful tool for the study of problems in chemistry and materials science. The main advantages of this method are the fact that it requires only the calculation of the forces, its numerical stability, and the quality of the trajectories. Furthermore, the method lends itself to very efficient parallelization, and it can include naturally the multiple timescale approaches [169].

4.3. Escaping Free-Energy Minima

For many systems, the free-energy surface (FES) may have multiple local minima separated by large barriers; therefore, the timescale that typical MD and MC simulations can reach is severely limited. Examples of such systems include conformational changes in solution, protein folding, and many chemical reactions. A large number of methods have been developed to overcome the problem, some of which were already mentioned in Sections 4.1 and 4.2

(see, e.g., the accelerated dynamics approach [138] or the dynamical transition path sampling method [160]).

Recently, a novel and powerful method for exploring the properties of multi-dimensional FES of complex systems was proposed by Laio and Parrinello [170]. This method combines the ideas of coarse-grained dynamics on the FES [171, 172] with those of adaptive bias potential methods [173, 174]. The method allows the system to escape from local minima in the FES and at the same time achieves a quantitative determination of the FES through the integrated process. This method assumes that there exist a finite number of relevant collective coordinates s_i, $i = 1, n$, where n is a small number, and that the free energy $\mathscr{F}(s)$ depends on these parameters. The exploration of the FES is guided by the generalized forces $F_i^t = -\partial \mathscr{F}/\partial s_i^t$. To estimate the forces more efficiently, an ensemble of P replicas of the system is introduced, each obeying the constraint that the collective coordinates have a preassigned value $s_i = s_i^t$. The coarse-grained dynamics of the collective coordinates is defined as follows:

$$\sigma_i^{t+1} = \sigma_i^t + \delta\sigma \frac{\phi_i^t}{|\phi^t|} \tag{30}$$

where $\sigma_i^t = s_i^t/\Delta s_i$ and $\phi_i^t = F_i^t \Delta s_i$ are the scaled collective coordinates and forces, respectively. The variable Δs_i is the estimated size of the FES well in the direction s_i, $|\phi^t|$ is the modulus of the nth dimensional vector ϕ_i^t, and $\delta\sigma$ is a dimensionless stepping parameter. After the collective coordinates are updated using Eq. (30), a new ensemble of replicas of the system with values σ_i^{t+1} is prepared, and new forces F_i^{t+1} are calculated for the next iteration. At the same time, the driving forces are evaluated from the microscopic Hamiltonian in short, standard microscopic MD runs. To explore the FES more efficiently, the forces in Eq. (30) are replaced by a history-dependent term

$$\phi_i \rightarrow \phi_i - \frac{\partial}{\partial \sigma_i} W \sum_{t' \leq t} \prod_i e^{-\frac{|\sigma_i - \sigma_i^{t'}|^2}{2(\delta\sigma)^2}} \tag{31}$$

where the height and the width of the Gaussian, W and $\delta\sigma$, are chosen to provide a reasonable balance between accuracy and efficiency in exploring the FES. The component of the forces coming from the Gaussian will discourage the system from revisiting the same spot and will encourage an efficient exploration of the FES. As the system diffuses though the FES, the Gaussian potentials accumulate and fill the FES well, allowing the system to migrate from well to well. After a while, the sum of the Gaussian terms will almost exactly compensate the underlying FES well [170].

A typical example of this behavior can be seen in Fig. 7, in which the dynamics in Eq. (30) are used to explore a one-dimensional PES $\mathscr{V}(s)$ with three wells. The dynamics start from a local minimum that is filled by the Gaussians in ~ 20 steps. Then the dynamic escapes from the well from the lowest-energy saddle point, filling the second well in ~ 80 steps. The second-highest saddle point is reached in ~ 160 steps, and the full PES is filled in a total of ~ 320 steps. Hence, in the case of this example, because the form of the potential is known, it can be verified that for large t and small $\delta\sigma$

$$-\sum_{t' \leq t} W e^{-\frac{|\sigma - \sigma t'|^2}{2(\delta\sigma)^2}} \rightarrow \mathscr{V}(s) \tag{32}$$

modulo an additive constant. Laio and Parrinello also suggest that Eq. (32) holds for a FES, and the free energy can be estimated from Eq. (32) for large t [170]. The efficiency of the method in filling a well in the PES or the FES can be estimated by the number of Gaussians that are needed to fill the well. This number is proportional to $(1/\delta\sigma)^n$, where n is the dimensionality of the problem. Hence, the efficiency of the method scales exponentially with the number of dimensions involved. A judicious choice of Δs_i, W, and $\delta\sigma$ will ensure the right balance between accuracy and sampling efficiency, and the optimal height and width of the Gaussians can be determined by the typical variations of the FES.

The method has been applied to the study of dissociation of a NaCl molecule in water and of the isomerization of alanine dipeptide in water [170]. Overall, the method is very efficient
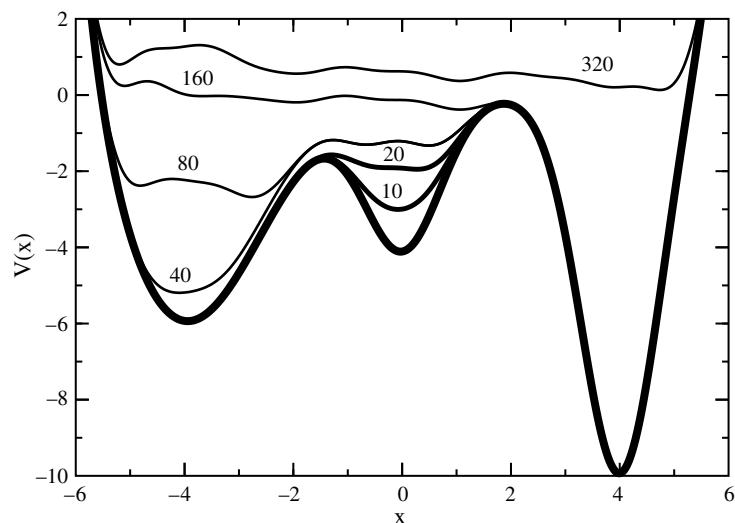
Figure 7. Time evolution of the sum of a one-dimensional model potential $V(\sigma)$ and the accumulating Gaussian terms of Eq. (31). The dynamic evolution (thin lines) is labeled by the number of dynamical iterations in Eq. (30). The starting potential (thick line) has three minima, and the dynamics are initiated in the second minimum.

in exploring the FES of complex systems if the collective coordinates are chosen judiciously. In particular, the topology of a FES can usually be determined by a few coarse-grained dynamics steps using "large" Gaussians. Subsequently, the qualitative knowledge of the FES can be improved using "smaller" Gaussians, effectively reducing the dimensionality of the problem by exploiting the topological information obtained with "large" Gaussians. As we alluded earlier, the current method assumes that the free energy $\mathcal{F}(s_i)$ depends on a small number of collective coordinates s_i. However, it is not always obvious or possible to identify such collective coordinates for complex systems *a priori*. In the example of isomerization of alanine dipeptide in water, Laio et al. chose the dihedral angles Φ and Ψ as the collective coordinates to explore the FES. These authors recognized that the dihedral angles alone do not provide the complete description of the dialanine isomerization reaction and that the real reaction coordinates should include the solvent degrees of freedom. However, their results seemed to reproduce the essential features of the FES; therefore, the authors concluded that the neglected degrees of freedom, although relevant for determining the reaction coordinates, are associated with small free-energy barriers and are sampled efficiently during the microscopic dynamics of the dihedral angles Φ and Ψ. Despite the success of this particular example, identifying a small number of collective coordinates *a priori* remains challenging within this approach. Moreover, the exploration of the FES would be more efficient if an adaptive way of determining the parameters of Gaussians could be developed.

4.4. Other Methods

For systems with a natural disparity in inherent timescales, various multiple-time-step integration algorithms have been developed to deal with them more efficiently [175–177]. One well-known example of such strategy is the Born–Oppenheimer approximation, in which the electron motion is separated from that of the nuclei because of the large disparity between their masses. In general, the separation of timescales occurs when some subset of forces present in the system is much stronger compared to the rest of the forces, while the masses of the constituents are about the same. For example, in the simulations of the polyatomic liquids with flexible bonds, the bond vibrations usually occur at a much faster rate than bond translation and rotations. In such systems, the configuration space can be divided into fast and slow degrees of freedom, with the force also being separated into fast and slow components. This separation yields a set of coupled equations of motion for the evolution of the fast and slow degrees of freedom. Instead of solving this set of equations simultaneously, multiple-time-step integration uses a small time step δt to advance the fast degrees

of freedom n steps holding the slow variables fixed. The slow degrees of freedom are then updated using a time step $n\delta t$. The variable n can be chosen typically between 5 and 10 steps in MD simulations of molecules that can be described in this way. Furthermore, if an analytic solution of high-frequency motion can be found, this solution can be incorporated into an integration scheme for the whole system, such that a time-step characteristic of the slow degrees of freedom can be used and the system simulated effectively with a much smaller number of cycles [177].

Recently, a method based on optimization of the action functional was proposed to extend the timescale of MD simulations by several orders of magnitude [178]. In this method, instead of parameterizing the trajectory as a function of time, the trajectory is parametrized as a function of length. Instead of solving the Newton equations in MD simulations, an action term (stochastic difference equation with respect to time) is optimized. For activated processes, the method eliminates the "incubation time," and has proven to be very efficient in the simulations of biomolecules. It remains to be seen, however, whether the method can be applied to problems in materials science.

5. CONCLUSIONS

In this chapter we have attempted to provide a comprehensive, if not exhaustive, overview of the current status of multiscale simulations methods and their applications in materials science. We divided the methods that address multiscale problems in the spatial regime into sequential and concurrent methods.

The sequential multiscale modeling techniques are, in general, more efficient computationally, but they depend on *a priori* knowledge of physical quantities of interest, such as the γ-surface in the P-N model, the free energies in the phase–field model, and atomistic local laws for mesoscopic DD simulations. The relevance of these quantities to the coarse-grained models needs to be carefully examined before the application of the methods. Furthermore, these approaches should only be pursued when phenomenological theories (such as the P-N model or the phase–field model) are well established; therefore, the methods are restricted in their range of application. In particular, these phenomenological models are often associated with the assumption of locality (both in space and time). The example of a local approximation in the phase–field model is embodied in Eq. (10), which assumes that part of the energetics of an inhomogeneous system can be written in terms of quantities obtained for homogeneous systems [1]. Similarly, in the P-N model, the γ-energy is assumed to be constant within Δx distance [see Eq. (7)] to evaluate the total misfit energy. The static approximation (locality in time) for dynamic properties is also widely used in phenomenological models. The coupling between different scales in a sequential approach is usually implicit. A successful sequential simulation depends equally on the reliability of the phenomenological model and on the accuracy of the relevant parameters entering the model.

The concurrent multiscale approaches are much more complicated and computationally demanding, but they do not require *a priori* knowledge of physical quantities supplied from distinct, lower-scale simulations. Furthermore, concurrent approaches do not depend on any phenomenological models; therefore, they are of more general applicability. Although concurrent approaches are more desirable and appealing, the actual problem to be attacked must be carefully posed to make the method practical. The problems that may arise in a concurrent approach are usually associated with the partition of domains in the system. For example, one needs to dynamically track the domain boundaries in the MAAD simulations and to adapt the FE meshes in the quasicontinuum simulations, both of which require additional care and computational resources. More important, in contrast to a sequential method, a "good" handshaking in a concurrent approach between different domains is both challenging and critical. Although some interesting ideas have been proposed to remedy the problems of coupling between different domains, such as the reflection of phonons at the domain interface [179–181], there is no general consensus on what a proper coupling of domains is. A general criterion that measures the quality of handshaking between domains would therefore be desirable. There is plenty of room for innovative research on the issue

of domain coupling. General mathematical formulations of multiscale problems, including error estimation, may turn out to be very useful for practical simulations [172, 182]. In our view, a successful concurrent approach usually has to satisfy three conditions. First, solve the coupled problem (Hamiltonian) accurately and efficiently by using ideas such as coarse-graining, "bonding energy partition," or "embedding potential." Second, the separate models employed in different domains of the system ought to be compatible (i.e., the physical description of the system resulting from the distinct models should be as close as possible). Third, at each level, the individual model should provide a good description of its assigned domain. We wish to emphasize the importance of the second condition that is not in general well recognized. The first condition usually guarantees a "smooth" handshaking across two domains (e.g., the electron density distribution or the displacement field varies smoothly across the interface), but nonphysical charge transfer or atomic relaxation at the interface could occur if the second condition is not satisfied. Therefore, a "smooth" handshaking does not constitute a "good" handshaking, and a successful concurrent approach relies on handshakings that are both mathematically accurate and physically consistent.

In this overview, we have also described a number of approaches that strive to extend the temporal scale in the modeling and simulation of material properties. We categorized these approaches to methods for accelerating the dynamics, methods for finding transition paths between equilibrium structures, and methods for escaping free-energy minima. Although these approaches represent very significant developments in the field, the problem of linking the timescale of atomic motion and vibrations (on the order of order femtoseconds) to scales at which interesting physical phenomena are typically studied (microseconds and beyond) is still wide open in many respects.

Because of the tremendous and continuing progress in multiscale strategies, this review is by no means exhaustive. We hope that we have conveyed the message that multiscale modeling is a truly vibrant enterprise of multidisciplinary nature. It combines the skills of physicists, materials scientists, chemists, mechanical and chemical engineers, applied mathematicians, and computer scientists. The marriage of disciplines and the concomitant dissolution of traditional barriers between them represent the true power and embody the great promise of multiscale approaches for enhancing our understanding of, and our ability to control, complex physical phenomena.

ACKNOWLEDGMENTS

REFERENCES

1. R. Phillips, "Crystals, Defects and Microstructures—Modeling Across Scales." Cambridge University Press, Cambridge, 2001.
2. E. Kaxiras and S. Yip (Guest Editors), *Curr. Opin. Solid State Mater. Sci.* 3, 523 (1998) and accompanying articles.
3. T. Diaz de la Rubia and V. V. Bulatov (Guest Editors), *MRS Bull.* 26, 169 (2001) and accompanying articles.
4. S. Yip, *Nature Mater.* 2, 3 (2003).
5. W. M. C. Foulkes, L. Mitas, R. J. Needs, and G. Rajagopal, *Rev. Mod. Phys.* 73, 33 (2001).
6. A. Szabo, N. S. Ostlund, "Modern Quantum Chemistry." McGraw-Hill, New York, 1989.
7. P. Hohenberg and W. Kohn, *Phys. Rev.* 136, B864 (1964); W. Kohn and L. Sham, *ibid*. 140, A1133 (1965).
8. M. C. Payne, M. P. Teter, D. C. Allan, T. A. Arias, and J. D. Joannopoulos, *Rev. Mod. Phys.* 64, 1045 (1992).
9. S. Goedecker, *Rev. Mod. Phys.* 71, 1085 (1999).
10. L. Colombo, *Comput. Mater. Sci.* 12, 278 (1998).
11. M. Z. Bazant and E. Kaxiras, *Phys. Rev. Lett.* 77, 4370 (1996).
12. F. Ercolessi and J.B. Adams, *Europhys. Lett.* 26, 583 (1994).
13. F. F. Abraham, R. Walkup, H. Gao, M. Duchaineau, T. de la Rubia, and M. Seager, *Proc. Natl. Acad. Sci.* 99, 5777 (2002).

14. L. P. Kubin and G. R. Canova, *Scripta Metall. Mater.* 27, 957 (1992).
15. J. P. Hirth, M. Rhee, and H. M. Zbib, *J. Comput. Aided Mater. Des.* 3, 164 (1996).
16. K. W. Schwarz, *Phys. Rev. Lett.* 78, 4785 (1997).
17. A. Needleman, *Acta Mater.* 48, 105 (2000).
18. V. V. Bulatov, M. Tang, and H. M. Zbib, *MRS Bull.* 26, 191 (2001).
19. M. Rhee, H. M. Zbib, J. P. Hirth, H. Huang, and T. de la Rubia, *Model. Simul. Mater. Sci. Eng.* 6, 467 (1998).
20. T. J. R. Hughes, "The Finite Element Method." Prentice-Hall, Englewood Cliffs, NJ, 1987.
21. P. R. Dawson and E. B. Marin, *Adv. Appl. Mech.* 34, 77 (1998).
22. T. Ohashi, *Philo. Mag. Lett.* 75, 51 (1997).
23. D. G. Pettifor and I. I. Oleinik, *Phys. Rev. Lett.* 84, 4124 (2000).
24. D. G. Pettifor, *Phys. Rev. Lett.* 63, 2480 (1989).
25. F. Abraham, J. Broughton, N. Bernstein, and E. Kaxiras, *Comput. Phys.* 12, 538 (1998).
26. J. Broughton, F. Abraham, N. Bernstein, and E. Kaxiras, *Phys. Rev. B* 60, 2391 (1999).
27. E. Clementi, *Philos. Trans. R. Soc. London A* 326, 445 (1988).
28. "Computational and Mathematical Models of Microstructural Evolution" (J. W. Bullard, L. Q. Chen, R. K. Kalia, and A. M. Stoneham, Eds.). Mater. Res. Soc. Proc. 529, Warrendale, PA, 1998.
29. "Multiscale Modeling of Materials" (V. V. Bulatov, T. Diaz de la Rubia, R. Phillips, E. Kaxiras, and N. Ghoniem, Eds.). Mater. Res. Soc. Proc. 538, Warrendale, PA, 1999.
30. "Multiscale Phenomena in Materials—Experiments and Modeling" (I. M. Robertson, D. H. Lassila, B. Devincre, and R. Phillips, Eds.). Mater. Res. Soc. Proc. 578, Warrendale, PA, 2000.
31. "Multiscale Modeling of Materials—2000" (L. P. Kubin, J. L. Bassani, K. Cho, H. Gao, and R. L. B. Selinger, Eds.). Mater. Res. Soc. Proc. 653, Warrendale, PA, 2001.
32. G. H. Campbell, S. M. Foiles, H. Huang, D. A. Hughes, W. E. King, D. H. Lassila, D. J. Nikkel, T. Diaaz de la Rubia, J. Y. Shu, and V. P. Smyshlyaev, *Mater. Sci. Eng. A* 251, 1 (1998).
33. W. E and B. Engquist, Notices of the AMS, 50, 1062 (2003).
34. M. S. Duesbery and G. Y. Richardson, *CRC Crit. Rev. Solid State Mater. Sci.* 17, 1 (1991).
35. V. Vitek, *Prog. Mater. Sci.* 36, 1 (1992).
36. B. Joós, Q. Ren, and M. S. Duesbery, *Phys. Rev. B* 50, 5890 (1994).
37. B. Joós and M. S. Duesbery, *Phys. Rev. Lett.* 78, 266 (1997).
38. Y. Juan and E. Kaxiras, *Philos. Mag. A* 74, 1367 (1996).
39. J. Hartford, B. von Sydow, G. Wahnström, and B. I. Lundqvist, *Phys. Rev. B* 58, 2487 (1998).
40. B. von Sydow, J. Hartford, and G. Washnström, *Comput. Mater. Sci.* 15, 367 (1999).
41. N. I. Medvedeva, O. N. Mryasov, Y. N. Gornostyrev, D. L. Novikov and A. J. Freeman, *Phys. Rev. B* 54, 13506 (1996).
42. O. N. Mryasov, Y. N. Gornostyrev, and A. J. Freeman, *Phys. Rev. B* 58, 11927 (1998).
43. V. V. Bulatov and E. Kaxiras, *Phys. Rev. Lett.* 78, 4221 (1997).
44. G. Lu, N. Kioussis, V. V. Bulatov, and E. Kaxiras, *Phys. Rev. B* 62, 3099 (2000); *Philos. Mag. Lett.* 80, 675 (2000).
45. G. Lu, Q. Zhang, N. Kioussis, and E. Kaxiras, *Phys. Rev. Lett.* 87, 095501 (2001).
46. G. Lu and E. Kaxiras, *Phys. Rev. Lett.* 89, 105501 (2002).
47. G. Lu, V. V. Bulatov, and N. Kioussis, *Phys. Rev. B* 66, 144103 (2002).
48. R. Peierls, *Proc. Phys. Soc. London* 52, 34 (1940).
49. F. R. N. Nabarro, *Proc. Phys. Soc. London* 59, 256 (1947).
50. V. Vitek, *Philos. Mag.* 18, 773 (1968).
51. J. D. Eshelby, *Philos. Mag.* 40, 903 (1949).
52. J. P. Hirth and J. Lothe, "Theory of Dislocations," 2nd ed. Wiley, New York, 1992.
53. S. M. Myers et al., *Rev. Mod. Phys.* 64, 559 (1992), and references therein.
54. G. Lu, D. Orlikowski, I. Park, O. Politano, and E. Kaxiras, *Phys. Rev. B* 65, 064102 (2002).
55. G. Xu, A. S. Argon, and M. Ortiz, *Philos. Mag. A* 75, 341 (1997).
56. J. R. Rice, *J. Mech. Phys. Solids* 40, 239 (1992); J. R. Rice, G. E. Beltz, and Y. Sun, in "Topics in Fracture and Fatigue" (A. S. Argon, Ed.). Springer, Berlin, 1992.
57. U. V. Waghmare, V. Bulatov, E. Kaxiras, and M. S. Duesbery, *Mater. Sci. Eng. A* 261, 147 (1999).
58. U. V. Waghmare, E. Kaxiras, V. Bulatov, and M. S. Duesbery, *Model. Simul. Mater. Sci. Eng.* 6, 483 (1998).
59. P. Peralta, S. A. Maloy, F. Chu, J. J. Petrovic, and T. E. Mitchell, *Scripta Mater.* 37, 1599 (1997).
60. Z. Suo, *Adv. Appl. Mech.* 33, 193 (1997).
61. A. Cocks and S. Gill, *Adv. Appl. Mech.* 36, 81 (1999).
62. M. Gurtin, *Physica D* 92, 178 (1996).
63. J. Bullard, E. Garboczi, and W. Carter, *J. Appl. Phys.* 83, 4477 (1998).
64. D. Fan and L. Q. Chen, *Philos. Mag. Lett.* 75, 187 (1997).
65. L. Q. Chen, C. Wolverton, V. Vaithyanathan, and Z. K. Liu, *MRS Bull.* 26, 197 (2001).
66. V. Vaithyanathan, C. Wolverton, and L. Q. Chen, *Phys. Rev. Lett.* 88, 125503 (2002).
67. Y. Z. Wang, L. Q. Chen, and A. G. Khachaturyan, in "Computer Simulation in Materials Science— Nano/Meso/Macroscopic Space and Time Scales" (H. Kirchner, L. Kubin, and V. Pontikis, Eds.). NATO ASI Series, Ile d'Oleron, France, 1995.
68. L. Q. Chen and Y. Z. Wang, *JOM* 48, 13 (1996).
69. D. Y. Li and L. Q. Chen, *Acta Mater.* 46, 2573 (1998).
70. A. G. Khachaturyan, "Theory of Structural Transformations in Solids." John Wiley, New York, 1983.

71. J. W. Cahn, *Acta Metall.* 9, 795 (1961).
72. P. C. Hohenberg and B. I. Halperin, *Rev. Mod. Phys.* 49, 435 (1977).
73. A. Zunger, in "Statics and Dynamics of Alloy Phase Transformations" (P. E. A. Turchi and A. Gonis, Eds.), p. 361. NATO ASI Series, Plenum, New York, 1994.
74. D. de Fontaine, *Solid State Phys.* 47, 33 (1994).
75. C. Wolverton, *Philos. Mag. Lett.* 79, 683 (1999); *Model. Simul. Mater. Sci. Eng.* 8, 323 (2000).
76. D. B. Laks, L. G. Ferreira, S. Froyen, and A. Zunger, *Phys. Rev. B* 46, 12587 (1992).
77. L. Kaufman and H. Bernstein, "Computer Calculation of Phase Diagrams with Special Reference to Refractory Metals." Academic Press, New York, 1970.
78. N. Saunders and A. P. Miodownik, "CALPHAD: A Comprehensive Guide." Pergamon, Oxford, 1998.
79. P. J. Spencer, *MRS Bull.* 24, 18 (1999).
80. D. Kandel and E. Kaxiras, *Solid State Phys.* 54, 219 (2000).
81. P. Kratzer and M. Scheffler, *Comput. Sci. Eng.* 3, 16 (2001).
82. W. Cai, V. V. Bulatov, J. F. Justo, S. Yip, and A. S. Argon, *Phys. Rev. Lett.* 84, 3346 (2000).
83. C. Ratsch, M. F. Gyure, R. E. Caflisch, M. Petersen, M. Kang, J. Garcia, and D. D. Vvedensky, *Phys. Rev. B* 65, 195403 (2002).
84. M. F. Gyure, C. Ratsch, B. Merriman, R. E. Caflisch, S. Osher, J. Zinck, and D. D. Vvedensky, *Phys. Rev. E* 58, 6927 (1998).
85. S. Osher and J. A. Sethian, *J. Comput. Phys.* 79, 12 (1988).
86. C. W. Shu and S. Osher, *J. Comput. Phys.* 83, 32 (1989).
87. C. S. Deo, D. J. Srolovitz, W. Cai and V. V. Bulatov, to be published.
88. V. Bulatov, F. F. Abraham, L. Kubin, B. Devincre and S. Yip, *Nature* 391, 669 (1998).
89. A. Needleman and E. Van der Giessen, *MRS Bull.* 26, 211 (2001).
90. F. Stillinger and T. A. Weber, *Phys. Rev. B* 31, 5262 (1985).
91. N. Bernstein and E. Kaxiras, *Phys. Rev. B* 56, 10488 (1997).
92. K. Ohsawa and E. Kuramoto, *J. Appl. Phys.* 86, 179 (1999).
93. F. F. Abraham and H. Gao, *Phys. Rev. Lett.* 84, 3113 (2000).
94. S. J. Zhou, P. S. Lomdahl, R. Thomson, and B. L. Holian, *Phys. Rev. Lett.* 76, 2318 (1996).
95. B. L. Holian and R. Ravelo, *Phys. Rev. B* 51, 11275 (1995).
96. P. Gumbsch, S. J. Zhou, and B. L. Holian, *Phys. Rev. B* 55, 3445 (1997).
97. S. J. Carroll, P. D. Nellist, R. E. Palmer, S. Hobday, and R. Smith, *Phys. Rev. Lett.* 84, 2654 (2000).
98. M. Moseler, J. Nordiek, and H. Haberland, *Phys. Rev. B* 56, 15439 (1997).
99. N. Choly and E. Kaxiras, *Solid State Comm.* 121, 281 (2002).
100. S. Watson, and E. Carter, *Comput. Phys. Comm.* 128, 67 (2000).
101. S. Kohlhoff, P. Gumbsch, and H. F. Fischmeister, *Philos. Mag. A* 64, 851 (1991).
102. P. Gumbsch, *J. Mater. Res.* 10, 2897 (1995).
103. E. B. Tadmor, M. Ortiz, and R. Phillips, *Philos. Mag. A* 73, 1529 (1996).
104. E. B. Tadmor, R. Phillips, and M. Ortiz, *Langmuir* 12, 4529 (1996).
105. V. B. Shenoy, R. Miller, E. B. Tadmor, R. Phillips, and M. Ortiz, *Phys. Rev. Lett.* 80, 742 (1998).
106. R. Miller, E. B. Tadmor, R. Phillips, and M. Ortiz, *Model. Simul. Mater. Sci. Eng.* 6, 607 (1998).
107. R. Miller, M. Ortiz, R. Phillips, V. Shenoy, and E. B. Tadmor, *Eng. Fracture Mech.* 61, 427 (1998).
108. D. Rodney and R. Phillips, *Phys. Rev. Lett.* 82, 1704 (1999).
109. V. B. Shenoy, R. Miller, E. B. Tadmor, D. Rodney, R. Phillips, and M. Ortiz, *J. Mech. Phys. Solid* 47, 611 (1999).
110. E. B. Tadmor, R. Miller, R. Phillips, and M. Ortiz, *J. Mater. Res.* 14, 2233 (1999).
111. V. B. Shenoy, R. Phillips, and E. B. Tadmor, *J. Mech. Phys. Solid* 48, 649 (2000).
112. G. S. Smith, E. B. Tadmor, and E. Kaxiras, *Phys. Rev. Lett.* 84, 1260 (2000).
113. J. Knap and M. Ortiz, *J. Mech. Phys. Solid* 49, 1899 (2001).
114. G. S. Smith, E. B. Tadmor, N. Bernstein, and E. Kaxiras, *Acta Mater.* 49, 4089 (2001).
115. V. Shenoy, V. Shenoy, and R. Phillips, in "Multiscale Modeling of Materials," (V. V. Bulatov, T. Diaz de la Rubia, R. Phillips, E. Kaxiras, and N. Ghoniem, Eds.), p. 465. Mater. Res. Soc. Symp. Proc. 538, Warrendale, PA, 1999.
116. A. H. King and D. A. Smith, *Acta Crystallogr. A* 36, 335 (1980).
117. E. B. Tadmor, G. S. Smith, N. Bernstein, and E. Kaxiras, *Phys. Rev. B* 59, 235 (1999).
118. E. B. Tadmor, U. V. Waghmare, G. S. Smith, and E. Kaxiras, *Acta Mater.* 50, 2989 (2002).
119. R. E. Rudd and J. Q. Broughton, *Phys. Rev. B* 58, R5893 (1998).
120. R. E. Rudd and J. Q. Broughton, *Phys. Stat. Sol.* 217, 251 (2000).
121. R. E. Rudd and J. Q. Broughton (unpublished).
122. S. Curtarolo and G. Ceder. *Phys. Rev. Lett.* 88, 255504 (2002).
123. A. A. Migdal, *Zh. Eksp. Teor. Fiz.* 69, 1457 (1975); L. P. Kadanoff, *Ann. Phys. (N.Y.)* 100, 259 (1968).
124. L. E. Shilkrot, R. E. Miller, and W. A. Curtin, *Phys. Rev. Lett.* 89, 025501 (2002).
125. E. van der Giessen and A. Needleman, *Model. Simul. Mater. Sci. Eng.* 3, 689 (1995).
126. N. Bernstein and D. Hess, *Mat. Res. Soc. Symp. Proc.* 653, Z2.7.1 (2001).
127. E. Lidorikis, M. Bachlechner, R. K. Kalia, A. Nakano, P. Vashishta, and G. Z. Voyiadjis, *Phys. Rev. Lett.* 87, 086104 (2001).
128. C. Woodward and S. I. Rao, *Phys. Rev. Lett.* 88, 216402 (2002).
129. K. Kremer and F. Müller-Plathe, *MRS Bull.* 26, 205 (2001).

130. J. Gao, *Rev. Comput. Chem.* 7, 119 (1996).
131. Q. Cui, M. Elstner, E. Kaxiras, T. Frauenheim, and M. Karplus, *J. Phys. Chem. B* 105, 569 (2001).
132. M. Elstner, D. Porezag, G. Jungnickel, J. Elsner, M. Haugk, T. Frauenheim, S. Suhai, and D. Seifert, *Phys. Rev. B* 58, 7260 (1998).
133. B. R. Brooks, R. E. Burccoleri, B. D. Olafson, D. J. States, S. Swaminathan, and M. Karplus, *J. Compt. Chem.* 4, 187 (1983).
134. N. Govind, Y. A. Wang, A. J. R. da Silva, and E. A. Carter, *Chem. Phys. Lett.* 295, 129 (1998).
135. N. Govind, Y. A. Wang, and E. A. Carter, *J. Chem. Phys.* 110, 7677 (1999).
136. T. A. Wesolowski and A. Warshel, *J. Phys. Chem.* 97, 8050 (1993).
137. T. Kluner, N. Govind, Y. A. Wang, and E. A. Carter, *Phys. Rev. Lett.* 86, 5694 (2001).
138. A. F. Voter, F. Montalenti, and T. C. Germann, *Annu. Rev. Mater. Res.* 32, 321 (2002).
139. A. F. Voter, *J. Chem. Phys.* 106, 4665 (1997).
140. A. F. Voter, *Phys. Rev. Lett.* 78, 3908 (1997).
141. R. Marcelin, *Ann. Phys.* 3, 120 (1915).
142. E. Wigner, *Z. Phys. Chem. B* 19, 203 (1932).
143. H. Eyring, *J. Chem. Phys.* 3, 107 (1935).
144. P. Hanggi, P. Talkner, and M. Borkovec, *Rev. Mod. Phys.* 62, 251 (1990).
145. J. B. Anderson, *Adv. Chem. Phys.* 91, 381 (1995).
146. G. H. Vineyard, *J. Phys. Chem. Solid* 3, 121 (1957).
147. A. F. Voter, *Phys. Rev. B* 57, R13985 (1998).
148. M. Sørensen and A. F. Voter, *J. Chem. Phys.* 112, 9599 (2000).
149. R. Elber and M. Karplus, *Chem. Phys. Lett.* 139, 375 (1987).
150. H. Jonsson, G. Mills, and K. W. Jacobsen, in "Computer Simulation of Rare Events and Dynamics of Classical and Quantum Condensed-Phase Systems" (B. J. Berne, G. Ciccotti, and D. Coker, Eds.). World Scientific, Singapore, 1998.
151. G. Henkelman, G. Johannesson, and H. Jonsson, in "Progress on Theoretical Chemistry and Physics," (S. D. Schwartz, Ed.). Kluwer Academic Publishers, 2000.
152. H. C. Anderson, *J. Chem. Phys.* 72, 2384 (1980).
153. G. Henkelman, B. Uberuaga, and H. Jonsson, *J. Chem. Phys.* 113, 9901 (2000).
154. P. Maragakis, S. Andreev, Y. Brumer, D. Reichman, and E. Kaxiras, *J. Chem. Phys.* 117, 4651 (2002).
155. T. Rasmussen, K. W. Jacobsen, T. Leffers, O. B. Petersen, S. G. Srinivasan, and H. Jonsson, *Phys. Rev. Lett.* 79, 3676 (1997).
156. M. Villarba and H. Jonsson, *Surf. Sci.* 317, 35 (1994).
157. B. P. Uberuaga, M. Leskovar, A. P. Smith, H. Jonsson, and M. Olmstead, *Phys. Rev. Lett.* 84, 2441 (2000).
158. G. Mills and H. Jonsson, *Phys. Rev. Lett.* 72, 1124 (1994).
159. M. R. Sorensen, K. W. Jacobsen, and H. Josson, *Phys. Rev. Lett.* 77, 5067 (1996).
160. C. Dellago, P. G. Bolhuis, F. S. Csajka, and D. Chandler, *J. Chem. Phys.* 108, 1964 (1998).
161. P. G. Bolhuis, C. Dellago, and D. Chandler, *Faraday Discuss. Chem. Soc.* 110, 421 (1998).
162. P. G. Bolhuis, D. Chandler, C. Dellago, and P. L. Geissler, *Annu. Rev. Phys. Chem.* 53, 291 (2002).
163. W. E, W. Ren and E. Vanden-Eijnden, to be published.
164. D. Passerone and M. Parrinello, *Phys. Rev. Lett.* 87, 108302 (2001).
165. R. E. Gillilan and K. R. Wilson, *J. Chem. Phys.* 97, 1757 (1992).
166. K. Mueller, *Angew. Chem.* 19, 1 (1980).
167. C. Dellago, P. G. Bolhuis, and D. Chandler, *J. Chem. Phys.* 108, 9326 (1998).
168. R. Car and M. Parrinello, *Phys. Rev. Lett.* 55, 2471 (1985).
169. V. Zaloj and R. Elber, *Comput. Phys. Commun.* 128, 118 (2000).
170. A. Laio and M. Parrinello, *Proc. Natl. Acad. Sci.* 99, 12562 (2002).
171. I. G. Kevrekidis, C. Theodoropoulos, and C. W. Gear, *Computers and Chemical Engineering* (to be published).
172. W. E and B. Engquist, *Comm. Math Sci.* 1, 87 (2003).
173. T. Huber, A. E. Torda, and W. F. van Gunsteren, *J. Comput. Aided Mol. Design* 8, 695 (1994).
174. F. Wang and D. P. Landau, *Phys. Rev. Lett.* 86, 2050 (2001).
175. R. D. Swindoll and J. M. Haile, *J. Comput. Phys.* 53, 289 (1984).
176. O. Teleman and B. Jonsson, *J. Comput. Chem.* 7, 58 (1986).
177. M. E. Tuckerman, G. J. Martyna, and B. J. Berne, *J. Chem. Phys.* 93, 1287 (1990).
178. R. Elber, A. Ghosh, and A. Cardenas, *Acc. Chem. Res.* 35, 396 (2002).
179. W. Cai, M. de Koning, V. V. Bulatov, and S. Yip, *Phys. Rev. Lett.* 85, 3213 (2000).
180. W. E and Z. Huang, *Phys. Rev. Lett.* 87, 135501 (2001).
181. W. E and Z. Huang, *J. Comput. Phys.* 182, 234 (2002).
182. W. E, B. Engquist, and Z. Huang, *Phys. Rev. B* 67, 092101 (2003).